Photocatalytic Degradation of a Herbicide Namely Glyphosate and Hexazinone from the Surface Water which will be Used as Drinking Water via Polyaniline/ZnWO₄/WO₃ and Evaluation of Acute Toxicity Assays

RUKİYE ÖZTEKİN [a], DELİA TERESA SPONZA [a, *]

[a] Department of Environmental Engineering
Dokuz Eylül University
Tınaztepe Campus, 35160 Buca/Izmir,
TURKEY
* Corresponding Author

Abstract: - Polyaniline/Zinc tungsten oxide/Tungsten trioxide nanocomposites (PANI/ZnWO₄/WO₃ NCs) was prepared to remove glyphosate (GLP) and Hexazinone (HZN) herbicides from the surface water. The properties of PANI/ZnWO₄/WO₃ NCs was investigated using XRD, FTIR, FESEM, HRTEM, XPS analyses. The toxicity of NCs and treated wastewater were investigated using Microtox and *Daphnia magna* acute toxicity tests. The effects of increasing values of PANI/ZnWO₄/WO₃ NCs concentrations (0.1, 0.4, 0.6, 1.0 and 1.5 mg/l), PANI/ZnWO₄/WO₃ mass ratios (1:1:3, 1:2:3, 3:1:1 and 3:2:1), GLP concentrations (1, 2, 3 and 4 mg/l), photodegradation times (2, 10, 15 and 20 min), and solar light powers (20, 40, 60, 80 and 100 W/m²) on the GLP and HZN removals in the surface were examined. The results of the acute toxicity analysis performed showed that the acute toxicity in the surface water decreased significantly after photooxidation. The maximum removal conditions for 3 mg/l GLP (99.90%) were 1 mg/l PANI/ZnWO₄/WO₃ NCs with a PANI/ZnWO₄/WO₃ ratio of 1:2:3 after 15 min photodegradation time at 80 W/m² sun light power while the maximum HZN removal was obtained as 96% after 15 min photodegradation, under 300 W solar light, at pH=7.0 and at 25°C. The crystalline monoclinic ZnWO₄ and WO₃ was detected from XRD analysis while PANI exhibited characteristic broad peak at 28.91° with an amorphous nature. FTIR spectra showed that pure ZnWO₄ has the Zn–O–W vibrational bands. XPS analysis, exhibited reactive oxygen species. The charge/discharge analysis indicated that WO₃ has a larger particle size that decreases surface density increasing the interplanar spacing between atoms. The introduction of ZnWO₄ and WO₃ nanoparticles into the PANI matrix enhanced the surface of the PANI/ZnWO₄/WO₃ NC.

Key-Words: - Glyphosate; Hexazinone; *Daphnia magna* acute toxicity test; Herbicie; Microtox acute toxicity assay; Photocatalytic degradation process; Polyaniline/Zinc tungsten oxide/Tungsten trioxide nanocomposites; Surface water.

1 Introduction

The increasing of population and industrial discharges to the environment elevated the limits required for drinking water supply and large-scale food production,[1]. Under these conditions in order to decrease the primary productivity at an economically steady-state level, some of agrochemicals has been extensively used to remove the pesticides and herbicides, [2]. With the excess utilization of some anthropogenic compounds and as a result of excess industrialization, water pollution was elevated, [3]. Synthetic pesticides and herbicides are usually utilized in agricultural lands to protect the plants. The herbicides were resistant to biological degradation, and has high bio-accumulative capacity consisting from their physicochemical properties with long half-life of 10–20 years. Their bio magnification increasing in the ecosystems and in the humans, [4, 5]. Due to recalcitrant structure of pesticides their persistence in soil, wastewater, and surface water elevated excessively and cause to an environmental problem. They can contaminate the food chain, and can cause toxicity to human health, [6]. Due to their high stability, these compounds cannot be biodegraded. The recent studies showed that exposure to the aforementioned compounds

cause to hormonal changes in the immune system and as a results some neurological and cardiac disease and some neoplasms occurred, [7, 8]. In order to remove these organics adsorption and advanced oxidation processes (AOPs), including Fenton, photo-Fenton, heterogeneous photocatalysis, ozonation systems…etc, were used, [9-11]. AOPs are based on the generation of free radicals, e.g., hydroxyl ($^{\bullet}OH$) and superoxide ($^{\bullet}O_2^-$), having high oxidizing activities in aquatic systems and pollutants can be converted into lower molecular weight metabolites and inorganic compounds, [12, 13]. Heterogeneous photocatalysis is an advanced process through the photoactivation of a semiconductor via redox reactions under sun and UV ligths, [14]. This process is very efficient and promising for the degradation of organic pollutants including dyes, antibiotics, drugs and pesticides, [9, 15, 16]. Among the nanocomposites used, metallic nano-oxides; Zinc oxide (ZnO) and titanium dioxide (TiO_2) have been excesively employed due to their low toxicity, good availability, chemical stability, large surface area/porosity, and photo-corrosion, [17, 18]. Nano-adsorbents and nanocomposites were used for pesticide removal from wastewater for their simplicity of operation, relatively low cost and low energy requirements, [19], Furthermore they have high specific surface area, chemical/thermal stability, and affinity to organic pollutants, [20].

Glyphosate herbicide (GLP; N-phosphomethyl[glycine] or $C_3H_8NO_5P$), is metabolized by microorganisms into aminomethylphosphonic acid (AMPA, known as its most active metabolite) and methylphosphonic acid (MPA), [21-23]. After more than 40 years of global use, GLP has been classified as "probably carcinogenic" in humans by the International Agency for Research on Cancer (IARC). In 2019, United States federal health agency, the Agency for Toxic Substances and Disease Registry, [24], part of the Centers for Disease Control and Prevention, [25], determined that both cancer and non-cancer hazards derive from exposure to GLP and GLP-based herbicides.

Hexazinone (HZN) is an example of an atypical triazine herbicide used for control of woody plants in reforestation areas and for selective weed control in sugarcane, pineapple, and alfalfa. The degradation of HZN in the rat, alfalfa, and sugarcane was reported by Holt, [26]. The mass spectral identification of HZN metabolites isolated from rat urine and from sugarcane extracts was reported by Reiser et al., [26]. Established sugarcane plants grown in the greenhouse were treated by soil drench with 14C-HZN and harvested at plant maturity 6 months later.

The total radioactive residues in mature sugarcane were less than 0.1 ppm, and the intact parent was not detected, [26].

No more studies were found in the recent literature about the removal of GLP: For the degradation of GLP, ultimate and intermediate metabolites such as AMPA, sarcosine, formaldehyde and CO_2 was produced during microbial transformation. During abiotic degradation, the amounts of GLP degraded by non-microbial forms and biological transformation were negligible, [27]. Low GLP yields was detected in the biodegradability studies performed by microorganisms. The biodegradation of GLP in soils by microorganisms is also rapid, [28]. During the photodegradation of GLP by sunlight no GLP removals was detected in soils, [29]. Other some chemical and physicochemical methods are used with nanocomposites to degrade the GLP. TiO_2 photocatalyst with H_2O_2 under UV ligth provided 65-70% GLP removals. TiO_2 particles doped with Mn, Ce or La under visible light provided 79-83% GLP removals. A nanocomposite namely $BiOBr/Fe_3O_4$ consisting from TiO_2 nanotubes and photocatalytic Ce and Fe_3O_4 was used in GLP photooxidation. MnO_2 and $BiVO_4$ was used as nanocomposite for the removal of GLP, [30]. In addition, in the removal of GLP adsorption on a $MnFe_2O_4$-graphene hybrid compound and an oxidative degradation process assisted with MnO_2 has been used, [31]. However, in the aforementioned studies low GLP yields (79-82%) was detected. In recent years nnotechnology recently began to used to photodegrade the GLP with high yields. In the studies performed by MnO_2/C nanocomposite high GLP yields was detected (87%) due to high specific surface and high dispersion of the aforementioned nanocomposite, [28]. An efficient GLP removal was further achieved using a nanosized resin (D201Cu) modified with $Cu(OH)_2$), [32]. However, the GLP yields found in the study given above were not effectively high and remained between 76% and 81%, [32]. Degradation of HZN has been investigated by means of photocatalysis of mixed-phase crystal nano-TiO_2. Influences of adsorption, amount of nano-TiO_2, pH and irradiation time on the photocatalytic process are studied. Results show that hexazinone is totally degraded within 140 min of irradiation under pH neutral conditions, [33].

More than 98% degradation of HZN was observed under 3 J/cm^2 UVC (ultraviolet C) fluence in the presence of 0.5 mM H_2O_2 at pH 7.0, [34]. Moreover, the degradation rate enhanced significantly with an increase in the initial dosage of H_2O_2, UV fluence, and contact time in the UV/H_2O_2 process. The rate of degradation was lower using secondary effluent than

that of Milli-Q water due to the presence of dissolved organics in wastewater. However, the reactions in bothmatrices obeyed pseudo-first-order kinetics.

Photocatalytic kinetic information of HZN degradation exhibited first order kinetics from the fit in the Langmuir–Hinshelwood model with high yields (96%), [33].

Electrochemical degradation of HZN in aqueous solution was performed by using Bi-doped PbO_2 electrodes as anodes. The main influencing parameters on the electrocatalytic degradation of HZN were initial HZN concentration, current density, initial pH and Na_2SO_4 concentration. The electrochemical oxidization reaction of HZN fitted pseudo-first-order kinetics model with a yield of 95.9%, [35].

Polyaniline (PANI) is a conducting polymer and organic semiconductor of the semi-flexible rod polymer family, [36, 37]. PANI has low-cost and environment-friendly conjugated semiconductor for the fabrication and is effective under visible light photocatalysis, [38]. It is a conducting polymer with an extensive conjugated π-system and high absorption coefficient under visible light during charge carrier production. It has a simple processing with high conductivity during production of heterojunction nano catalysts. In recent studies many effective data were detected during photodegradation of organics when contacting with its interfaces and individual pollutant components. PAI exhibited high separation efficiency during photocatalysis for photogenerated electron–hole pairs, [39].

Zinc tungsten oxide or zinc tungstate ($ZnWO_4$) is extensively used during photodegradation due to its high UV light response, tunable band edges, optical transparency, chemical stability, and suitable strength, [40]. The band edge tuning of $ZnWO_4$-centered nanostructures can be organized through appropriate changes such as heterostructure construction, doped/combining with transition metal ions, and noble metals, [41, 42]. By deposition of O_2^- ions around the tungsten (W), $ZnWO_4$ forms an insulated trioxide-oxo-tungsten [WO_6] octahedron with an asymmetric shape showing a local atomic structure with a wolframite-type space group of P2/c, [43]. This is an essential inorganic ternary oxide material with crystalle properties and exhibited scheelite structure depending on the ionic radius, [44]. W clusters formed a network since they are more stable, leading to form the covalent nature of W–O bonds. During generation of electron-hole pairs a charge separation process was performed with dipoles when WO_6 clusters act as electron receptors. Thus, the oxygen vacancies in the Zn/W clusters can transfer electrons to the W cluster and permanent

dipoles were generated, [45]. The Zn and W vacancies act as electron capture in the holes since they are charged negatively, [46].

Tungsten trioxide (WO_3) is an n-type semiconductor photocatalyst having a wide range of bandgap values (2.7–3.4 eV) providing a better extension into the visible range, [47]. WO_3 as alone photocatalyst suffers from the limitation of fast recombination of charge carriers, thereby restricting its potential during photocatalytic applications, [48]. Several studies suggest that constructing a heterojunction between two metal oxides with suitable band arrangements can improve the charge carrier separation by suppressing the fast recombination, [49, 50]. Binary heterojunctions like WO_3/Bi_2WO_6, [51], WO_3/ZnO, [52], and WO_3/TiO_2, [53], have been constructed to achieve superior charge separation and high photocatalytic yields. Bimetallic W has always been very significance for its chemical inertness structure with low toxicity, exhibited corrosion-resisstant properties with large magnetic properties, and economic feasibility, [54]. $ZnWO_4$ possesses wolframite (WO_4) structures with six-fold coordination sites for W exhibited superior activities under UV light, [55].

The interaction of WO_3 with $ZnWO_4$ also provides high photocatalytic activity by changing the electronic properties in the material. WO_3 it can be recombinated fastly providing low charge carrier properties and leading to a lower photocatalytic degradation efficiency compared to other metal oxides such as TiO_2 or ZnO, [56]. Conversely, $ZnWO_4$ presents a high ionic conductivity and long lifetime of photogenerated carriers under sun ligth irradiation, [56].

PANI has received increasing attention due to its electron and hole transferring properties. It can be easily prepared with high chemical stability, [57]. Furthermore, many studies showed that combination of PANI with semiconductors impoved the interfacial charge carrier's separation due to the excellent charge carrier mobility and thus enhance the photo-electrocatalytic activity, [58]. With g-C_3N_4/PANI composite enhanced photocatalytic yields was detected for degradation of methylene blue (MB) dye, [59]. Wang et al., [60], synthesized $ZnWO_4$ modified by polyaniline (PANI/$ZnWO_4$) and found that the photocatalytic activity of PANI/$ZnWO_4$ composites was higher than $ZnWO_4$. This was attributed to the synergistic effect between PANI and $ZnWO_4$. $ZnWO_4$ nanosheets were homogenously grown on the surface of the WO_3 resulting in a large active surface area. The charge carriers separation can be improved because of the energy band structure

match between WO_3 and $ZnWO_4$. This improve significantly the photoelectrochemical activity, [60].

Barık et al., [61], investigated the degradation of the toxic GLP herbicide ($K_{app} = 0.0707$ min^{-1}). In this study, radical trapping experiment, and reactive oxygen species (ROS) quantification ($^{\bullet}OH$ and $^{\bullet}O_2^-$) suggested a possible double electron transfer type Z-scheme mechanism, which accounts for superior solar light-assisted N–C bond cleavage of GLP herbicide. Barık et al., [61], a ternary PANI–ZnWO$_4$–WO$_3$ photocatalyst was synthesized via in situ polymerization method exhibiting double Z-scheme channelization towards photodegradation of GLP with superior minimization of toxicity of degraded metabolites.

Based on the assumptions and references given above, in other to improve the removals of GLP and HZN herbicides from the surface water via photooxidation, in this study, PANI/ZnWO$_4$/WO$_3$ NCs were prepared under laboratory conditions. The influence of different PANI/ZnWO$_4$/WO$_3$ NCs concentrations (0.1, 0.4, 0.6, 1.0 and 1.5 mg/l), PANI/ZnWO$_4$/WO$_3$ mass ratios (1:1:3, 1:2:3, 3:1:1 and 3:2:1), GLP and HZN concentrations (1, 2, 3 and 4 mg/l), photodegradation times (2, 10, 15 and 20 min), and solar light powers (20, 40, 60, 80 and 100 W/m^2) on the photodegradation yields of GLP and HZN was examined. The characteristics of the synthesized NCs were assessed using XRD, FTIR, FESEM, HRTEM and XPS analyses, respectively. The ecotoxicities of NCs and treated wastewater were investigated using Microtox (*Aliivibrio fischeri*) and *Daphnia magna* acute toxicity tests.

2 Materials and Methods

2.1 Synthesis of ZnWO₄ Nanoparticles (NPs)

ZnWO$_4$ was prepared by 1-butyl-3-methylimidazolium chloride (BMIMCl) ionic liquid (IL)-assisted solvothermal method. In a typical procedure, 0.005 mole of Zn(NO$_3$)$_2$.6H$_2$O and the same amount of Na$_2$WO$_4$ was added to a 50 ml of deionized water and BMIMCl IL mixture solution. The whole reaction mixture was kept under mechanical stirring for 30 min. The pH of the solution was balanced at 3.0 before transferring the whole solution to the Teflon-lined stainless-steel autoclave. The reaction was kept at 180ºC for 18 h. After, the reaction was cooled at room temperature naturally. The white precipitates were washed with ethanol and deionized water followed by drying at 70ºC for 8 h before further characterization

2.2 Synthesis of WO₃ NPs

WO$_3$ was also prepared by BMIMCl IL-assisted solvothermal method. 0.005 mole of Na$_2$WO$_4$ was added to 50 ml of deionized water and BMIMCl IL mixture solution. The resultant reaction mixture was kept under mechanical stirring for 30 min. The pH of the solution was adjusted to 3.0 with 0.1 M HCl solution. The resultant mixture was transferred to the autoclave and it was kept at 180ºC for 18 h. Then, the reaction was cooled naturally. The final solid residue was washed with ethanol and deionized water followed by drying at 70ºC for 8 h before further characterization.

2.3 Synthesis of PANI

In chemical oxidation polymerization, PANI is synthesized by using hydrochloric acid (HCl) or sulfuric acid (H$_2$SO$_4$) as a dopant and ammonium persulfate [(NH$_4$)2S$_2$O$_8$] as an oxidant in an aqueous environment, [62, 63]. At this time, a proton can be removed by the oxidant from the monomer of aniline without either creating a heavy bond, or with the absolute product.

In chemical synthesis, there are three reactants of PANI that require aniline, oxidant, and acidic medium. HCl and H$_2$SO$_4$ are common acids used in the synthesis of PANI, whereas [(NH$_4$)2S$_2$O$_8$, hydrogen peroxide (H$_2$O$_2$), sodium vanadate (NaVO$_3$), cerium sulfate [Ce(SO$_4$)$_2$], potassium dichromate (K$_2$Cr$_2$O$_7$), potassium iodate (KIO$_3$), and potassium free cyanide {K$_3$[Fe(CN)$_6$]} can be used as oxidizers. The oxidant polymerization method is the most communal mechanism used to synthesize PANI, while aniline reacts with an acidic substance as a neutralizing agent and polymerizes by adding one drop of an oxidizing agent such as [(NH$_4$)2S$_2$O$_8$ at dissimilar temperatures. After realization, the polymerization mechanism (3 h) was an aqueous solution separated by filtration. Pure PANI can be obtained by rinsing the above solution 5–6 times with deionized water. Alcohol and acetone are then added to make the filter colourless and ensure that non-reactive materials are completely removed. The product is slime green and is well-known as PANI polymer aldine salt, which is unstable due to the existence of swords. Therefore, the polymer aldine salt converts to the PANI-EB structure, which is naturally stable at 25ºC, allowing this precipitate to equilibrate with and ensure that non-reactive materials, [64].

2.4 Synthesis of PANI/ZnWO₄/WO₃ NCs

The ternary PANI/ZnWO$_4$/WO$_3$ NCs was synthesized by an ionic liquid-assisted in situ oxidative polymerization process. In this process,

BMIMCI used in the polymerization of aniline using $[(NH_4)2S_2O_8]$. At the beginning, 0.8 ml of aniline was added to the aqueous solution of BMIMCI to determine three different PANI solutions. Then, in every PANI mixture, 0.2 mg/l $[(NH_4)2S_2O_8]$ was added at an $[(NH_4)2S_2O_8]$ to aniline ratio of 1/1. Furthermore, 0.31 g of $ZnWO_4$ and 0.21 g of WO_3 were dispersed in 50 ml of 0.15 M HCl solution during ultra sonication for 50 min. Then, the particle mixtures were transferred into the PANI mixtures and mixed at 21^oC. The dark green products were separated by centrifugation and washed with ethanol to remove the residual ionic part. The three composites (PANI/$ZnWO_4$/WO_3 NCs) obtained were dried in a vacuum oven at 60^oC.

2.5 Photocatalytic Degradation Reactor

A 2 liters cylinder quartz glass reactor was used for the photodegradation experiments of GLP and HZN aqueous solution at different operational conditions. 1000 ml of GLP and HZN aqueous solution was filled into a cylindrical quartz glass reactor, separately. Then, the photocatalyst was added into the cylindrical quartz glass reactors. The photocatalytic reactor was operated with constant stirring (1.5 rpm) during the photocatalytic degradation process. 10 ml of the reacting solution were sampled and centrifugated (at 10000 rpm) at different time intervals. Sunlight was used at hours 11.00, 12.30, 14.30 and 15.30 corresponding to increasing light powers of 20, 40, 60, 80 and 100 W/m^2, respectively.

2.6 GLP and HZN Photocatalytic Degradation Experiments

The photocatalytic degradation efficiencies of PANI, $ZnWO_4$ NPs, WO_3 NPs and PANI/$ZnWO_4$/WO_3 NCs were investigated with a cylinder quartz glass photocatalytic reactor under solar light irradiation. The series of GLP and HZN photodegradation studies were performed in aqueous solutions. The temperature of the photocatalytic system was maintained using a continuously circulating aqueous solution. Typically, 20 mg/l catalysts were used for the batch degradation study with 100 ml of 10 mg/l GLP and HZN nder continuous magnetic stirring in separate reactors. From 10 mg/l GLP and HZN stock solution, dilutions were performed for GLP and HZN concentrations of 1 mg/l, 2 mg/l, 3 mg/l and 4 mg/l in separate reactors. The pollutant solutions were maintained throughout the degradation process at pH=7.0 ± 0.1 by dropwise addition of 1.2 M H_2SO_4 and 1.2 M NaOH solutions as necessary. Initially, the reaction mixtures were kept in dark to check the adsorption properties of GLP and HZN to attain adsorption–desorption equilibrium. Next, the whole setup was exposed to solar light for the photocatalytic degradation study. In 20 min time gap, a 4 ml aliquot of the pollutant solution was withdrawn and centrifuged to separate the PANI/$ZnWO_4$/WO_3 NCs. The initial experimental conditions are given in Table 1.

* Table 1 can be found in the Appendix section.

The percentage degradation was calculated by the following Eq. (1):

$$\text{Degradation (\%)} = \left(\frac{C_o - C_t}{C_o}\right) \times 100 \qquad (1)$$

where; C_o: is the pollutant concentration before illumination, (mg/l) and C_t is the final concentration, (mg/l) of the pollutant at time t (min).

2.7 Determination of GLP and HZN

The quantification of GLP and HZN was determined with a gas chromatography (Agilent 8890N GC) equipped with a mass selective detector (Agilent MSD) Gas Chromatography-Mass Spectrometry (GC-MS) (Agilent 8890GC/Agilent MSD). A capillary column (HP5-MS, 30 m, 0.25 mm, 0.25 μm) was used. The injection volume was 1 μl. The initial oven temperature was kept at 50^oC for 1 min, then raised to 200^oC at 25^oC/min. Then the temperature was elevated from 200^oC to 300^oC at 8^oC/min for 6.5 min. High purity He(g) was used as the carrier gas at constant flow mode (1.8 ml/min, 48 cm/s linear velocity). The method involves the addition of 6% borate buffer to the aqueous sample to adjust the pH=9.3 and then mixing with 9-fluorenylmethyl chloroformate (FMOC) in acetonitrile (C_2H_3N) prior to analysis. The derivatization process was continued for 13 h at 23°C and the process was stopped by drop-wise addition of 7 M HCl solution where the resulting pH was measured to be pH=1.3. Chromatographic separation was performed with a C18 column where the mobile phase was 4 mM acetic acid/ammonium acetate (HAc/NH_4Ac) (pH=4.5) acetonitrile. The percentage of acetonitrile was changed from 75% (between 0th min and 40nd min) to 100% (between 40.1st min and 46th min) and then to 5% (between 46.1st min and 53th min). For each sample the separation process was completed in 30 min.

2.8 Photodegradation Mechanism of PANI/$ZnWO_4$/WO_3 NCs

Under the illumination of sunlight, the electrons in the valence band of PANI, $ZnWO_4$, and WO_3 are excited to their respective conduction bands leaving

Rukiye Öztekin, Delia Teresa Sponza

the photo-generated holes (h⁺) behind (Fig. 1). If the ternary composite follows photodegradation mechanism, the holes (h⁺) in the higher positive E_{VB} of ZnWO₄ and WO₃ migrate to the E_{VB} of PANI. On the other hand, the electrons (e⁻) migrate in reverse direction to the CB of ZnWO₄ and WO₃. The conduction band edge of ZnWO₄ and WO₃ located at - 0.23 and 0.45 eV which is insufficient to reduce O₂ into $O_2^{-\bullet}$ [E_0 ($O_2/O_2^{\bullet}$) = - 0.33 eV vs. NHE] (Fig. 1). Again, the photo-generated holes on the valence band of ZnWO₄ and WO₃ cannot lead to formation of OH$^\bullet$ from the OH⁻ ions/H₂O molecules [E_0 (OH⁻/OH$^\bullet$) = 1.99 eV vs. NHE, E_0 (H₂O/OH$^\bullet$) = 2.72 eV vs. NHE] (Fig. 1). This clearly banishes the formation $O_2^{-\bullet}$ from O₂ and the formation OH$^\bullet$ from the OH⁻ ions/H₂O molecules. But the radical trapping test and ROS quantification have already confirmed $O_2^{-\bullet}$ and OH$^\bullet$ as the major active species behind the photocatalytic degradation (Fig. 1). For this reason, the possibility of photodegradation mechanism has ruled out. These results were also supported by GC-MS analysis.

* Fig. 1 can be found in the Appendix section.

2.9 Characterization of Photocatalyst
2.9.1 X-Ray Diffraction (XRD) Analysis
Powder XRD patterns were recorded on a Shimadzu XRD-7000, Japan diffractometer using Cu Kα radiation (λ=1.5418 Å, 40 kV, 40 mA) at a scanning speed of 1º min⁻¹ at a 10-80º 2θ range. Raman spectrum was collected with a Horiba Jobin Yvon-Labram HR UV-Visible NIR (200-1600 nm) Raman microscope spectrometer, using a laser with a λ=512 nm. The spectrum was collected from 10 scans at a resolution of 2 cm⁻¹.

2.9.2 Fourier Transform Infrared Spectroscopy (FTIR) Analysis
The FTIR spectra of samples was recorded using a FT-NIR spectroscope (RAYLEIGH, WQF-510). Experimental samples were scanned using infrared light and their chemical properties were observed in FTIR spectra.

2.9.3 Field Emission Scanning Electron Microscopy (FESEM) Analysis
The morphological features and structure of the synthesized catalyst were investigated by FESEM (FESEM, Hitachi S-4700), to investigate the composition of the elements present in the synthesized catalyst.

2.9.4 High Resolution Transmission Electron Microscopy (HRTEM) Analysis
The structure of the samples was analyzed by HRTEM data. HRTEM analysis was recorded in a Technai G2 20 X-TWIN TEM (FEI, USA) under 200 kV accelerating voltage. Samples were prepared by applying one drop of the suspended material in ethanol onto a carbon-coated copper HRTEM grid and allowing them to dry at 25ºC.

2.9.5 X-Ray Photoelectron Spectroscopy (XPS) Analysis
The valence state of the samples was investigated and was analyzed using XPS (ESCALAB 250Xi, England). In XPS analysis it was used an Al Kα source and surface chemical composition and reduction state analyses was done by the core levels recorded using a pass energy of 30 eV (resolution≈0.10 eV). The peak fitting of the individual core-levels was done using XPS-peak 41 software, achieving better fitting and component identification. All binding energies were calibrated to the C 1s peak originating from C–H or C–C groups at 284.6 eV.

2.9.6 N₂-Adsorption-Desorption Curves
Micromeritics ASAP 2020 M porosimeter was used to measure the N₂-adsorption-desorption curves of the material. The supercapacitive behavior of the synthesized samples was investigated using Princeton Applied Research Center.

2.9.7 Band gap from the UV−vis absorbance
Detailed bandgap calculations were performed along with the proposal of an accelerated double electron transfer Z-scheme type channelization mechanism in the ternary heterojunction system.

The UV-DRS and photoluminescence (PL) spectra of the synthesized materials were recorded using Jasco V-650 spectrophotometer and Jasco FP-8200 Fluorescence spectrometer respectively.

2.9.8 AC Impedance Spectra and Electrochemical Impedance Spectroscopy (EIS) Analyses
The analysis of impedance data for reduction of ferricyanide [Fe(CN)₆]³⁻ in a potassium chloride (KCl) supporting electrolyte is used to demonstrate the error structure for impedance measurements, the use of measurement and the sensitivity of impedance to the evolution of nanocomposite properties.

2.9.9 Cyclic Voltammogram Records
Cyclic voltammetry is an electrochemical technique used to measure the current response of a redox active solution to a linearly cycled potential sweep using a

Henken potentiostat. It is a useful method if you need to quickly find information about the thermodynamics of redox processes and the energy levels of the nanocomposite.

2.9.10 Galvanostatic Charge/Discharge Curves

All electrochemical characterization was done using the Metrohm 128 N AUTOLAB Potentiostat from the Netherlands in 1 M KOH electrolyte.

2.10 Acute Toxicity Assays

Acute toxicity tests were applied to the raw surface water containing GLP and HZN, and to photodegraded surface water at maximum GLP and HZN removals was taken after treatment.

2.10.1 Microtox Acute Toxicity Test

Ecotoxicity to the bioluminescent organism *Aliivibrio fischeri* (also called *Vibrio fischeri*) was assayed using the Microtox measuring system according to DIN 38412L34, L341, (EPS 1/ RM/24 1992). Microtox testing was performed according to the standard procedure recommended by the manufacture, [65]. A specific strain of the marine bacterium, *V. fischeri*-Microtox LCK 491 Kit, [65], was used for the Microtox acute toxicity assay. Dr. LANGE LUMIX-mini type luminometer was used for the Microtox toxicity assay, [66].

2.10.2 *Daphnia magna* Acute Toxicity Test

To test ecotoxicity, 24-h born *Daphnia magna* were used as described in Standard Methods, [67], sections 8711A, 8711B, 8711C, 8711D and 8711E, respectively, [68]. After preparing the test solution, experiments were carried out using 5 or 10 *Daphnia magna* introduced into the test vessels. These vessels had 100 ml of effective volume at 7.0–8.0 pH, providing a minimum dissolved oxygen (DO) concentration of 6 mg/l at an ambient temperature of 20–25°C. Young *Daphnia magna* was used in the test (≤ 24 h old); 24–48 h exposure is generally accepted as standard for a *Daphnia magna* acute toxicity test. The results were expressed as mortality percentage of the *Daphnia magna*. Immobile animals were reported as dead *Daphnia magna*.

All experiments were carried out three times and the results are given as the means of triplicate samplings. The data relevant to the individual pollutant parameters are given as the mean with standard deviation (SD) values.

2.11 Statistical Analysis

Regression analysis between variables was performed using the EXCELL in Microsoft WindowsTM (HP, USA), [69]. The linear correlation was assessed with r^2. The r^2 value is the correlation coefficient and reflects statistical significance between dependent and independent variables. Analysis of variance (ANOVA) (SAS ANOVA procedure) test was used to assess the data obtained in reactors using the EXCELL in Microsoft WindowsTM (HP, USA), [69].

3 Results and Discussions
3.1 XRD Analysis Results

The results of XRD analysis for PANI, WO_3 NPs, $ZnWO_4$ NPs, PANI-WO_3 NCs, PANI-$ZnWO_4$ NCs and PANI/$ZnWO_4$/WO_3 NCs after photocatalytic degradation process during GLP removal was illustrated in Fig. 2. The characterization peaks were observed at a 2θ value of 27.88°, corresponding to the (002) for PANI (Fig. 2a). The characterization peaks were obtained at 2θ values of 22.17°, 39.97°, 53.25° and 55.11°, respectively, corresponding to the (001), (131), (100) and (112), respectively, for WO_3 NPs (Fig. 2b). The characterization peaks were found at 2θ values of 35.10°, 41.34° and 51.04°, respectively, corresponding to (110), (220) and (132), respectively, for $ZnWO_4$ NPs (Fig. 2c). The characterization peaks were observed at 2θ values of 25.61°, 40.36°, 55.47° and 58.79°, respectively, corresponding to (111), (033), (022) and (202), respectively, for PANI-WO_3 NCs (Fig. 2d). The characterization peaks were obtained at 2θ values of 28.75°, 30.11°, 40.42° and 51.65°, respectively, corresponding to the (124), (312), (021) and (121), respectively, for PANI-$ZnWO_4$ NCs (Fig. 2e). The characterization peaks were measured at 2θ values of 29.11°, 32.40°, 40.02°, 55.09° and 59.78°, respectively, corresponding to the (010), (225), (130), (103) and (211), respectively, for PANI/$ZnWO_4$/WO_3 NCs (Fig. 2f).

* Fig. 2 can be found in the Appendix section.

All the reflection peaks from the crystal planes are exhibited highly crystalline nature. The monoclinic crystal structure exhibited an agreement with the reported values in JCPDS file no.: 88-0251, with space group of $ZnWO_4$, [65]. From Fig. 2 it is seen that the monoclinic structural peak of $ZnWO_4$ indicates the crystalline nature in the whole composite. The bi-metal oxide $ZnWO_4$ also exhibited also a crystalline monoclinic-structure in the PANI matrix during chemical polymerization reaction.

3.2 FTIR Analysis Results

The FTIR spectrum of PANI, $ZnWO_4$ NPs and WO_3 NPs were determined after photocatalytic degradation process during GLP removal (Fig. 3). The main peaks of FTIR spectrum for PANI was observed at a wavenumber of 850 cm^{-1} (Fig. 3a). The main peaks of FTIR spectrum for $ZnWO_4$ NPs was obtained at 458 cm^{-1}, 570 cm^{-1} and 785 cm^{-1} wavenumbers, respectively (Fig. 3b) while the main peaks of FTIR spectrum for WO_3 NPs was determined at wavenumber of 740 cm^{-1} (Fig. 3c).

* Fig. 3 can be found in the Appendix section.

Prominent peaks and their assignment are found at 3434 cm^{-1} originated from NH bond-stretching while the maximum abundaces at 520 and 639 cm^{-1} are defined as Benzenoid and Quinoid ring bond stretching. The maximal disturbances at 725 cm^{-1} is N=H and + C-C bond-stretching. In the region of 631 cm^{-1}, 750 cm^{-1} and 1700 cm^{-1} the characteristic stretching maximums were defined as pure PANI and PANI/$ZnWO_4$ composites. Comparison of stretching frequencies of PANI and composites confirms that, frequencies of bond-stretching of the composites are sligtly elevated in the nano structure. This indicates a weak bond interaction between $ZnWO_4$ and PANI moeities. The peaks at 621 cm^{-1} and 629 cm^{-1} are stretching frequencies of metal and oxygen bond in pure $ZnWO_4$ composite. This strongly indicates the formation of PANI/$ZnWO_4$. The intensity of metal oxygen stretching peaks of FTIR spectra grows with increase in weight percent of $ZnWO_4$ in PANI.

3.3 FESEM Analysis Results

The morphological features of PANI, $ZnWO_4$ NPs, WO_3 NPs and PANI/$ZnWO_4$/WO_3 NCs were characterized through FESEM images (Fig. 4). The FESEM images of PANI, $ZnWO_4$ NPs, WO_3 NPs and PANI/$ZnWO_4$/WO_3 NCs were illustrated in Fig. 4a, 4b, 4c and 4d, respectively, after photocatalytic degradation of GLP and HZN.

* Fig. 4 can be found in the Appendix section.

Although, a spherical morphology was detected the nanocomposite particles exhibited cubic shapes. The average sizes of the NPs were 25 nm and 27 nm, respectively. Moreover, all metal oxide particles were well dispersed in the PANI matrix. In addition, the general morphology of all hybrid materials was found to be spherical.

3.4 HRTEM Analysis Results

The HRTEM images of PANI/$ZnWO_4$/WO_3 ternary NCs was performed to detect the micromorphological structure level after photocatalytic degradation process of GLP and HZN (HRTEM image scale: 220 nm) (Fig. 5).

* Fig. 5 can be found in the Appendix section.

High-resolution HRTEM images indicated the monocrystalline structure of the NCs. The HRTEM images demonstrate the polycrystalline structure of the investigated NCs, with average diameter of 21.9 ± 10 nm. The lattice distance of the NCs was 0.9 ± 0.03 nm corresponding to the (002) crystal planes. HRTEM images exhibited that a compact interface is formed between WO_3 nanorods and $ZnWO_4$ nanosheets. The lattice fringes was measured as 0.489 nm and 0.359 nm corresponding to the crystal planes (101) and (012) of the $ZnWO_4$ phase, respectively (data not shown). The lattice space of 0.379 nm is corresponded to the (003) planes of monoclinic WO_3. This indicates that WO_3 and Zn^{2+} were transformed into $ZnWO_4$ during in situ reaction. Such surface/interface are beneficial for the formation of oxygen vacancy, and also helpful for improving the electronic transmission. WO_3 nanorod indicates that the WO_3 have a single-crystalline structure with a diameter of 0.386 nm and can be attributed to the (002) plane defining the monoclinic WO_3. The pattern of the WO_3 confirmed the single-crystalline structure of WO_3. The data shows that (002) and (020) facets with an angle of 90° indicates the crystal structure of WO_3. This component is growing along the (100) direction (data not shown).

3.5 XPS Analysis Results

The XPS analysis of PANI, $ZnWO_4$ NPs, WO_3 NPs and PANI/$ZnWO_4$/WO_3 NCs were perforned during photo catalytic oxidation of GLP and HZN (Fig. 6). Absorption peaks were observed at binding energy of 396.14 eV for PANI (red line) (Fig. 6a), at 399.63 eV for $ZnWO_4$ NPs (green line) (Fig. 6b), at 402.91 eV for WO_3 NPs (blue line) (Fig. 6c) and at 398.36 eV for PANI/$ZnWO_4$/WO_3 NCs (black line) (Fig. 6d), respectively, after photocatalytic degradation of GLP.

* Fig. 6 can be found in the Appendix section.

The survey spectra of PANI, $ZnWO_4$ NPs, WO_3 NPs and PANI/$ZnWO_4$/WO_3 NCs exhibiting four peaks at 411, 399, 398.9, and 399 eV shows the existence of W, Zn, O, and C elements. Pristine $ZnWO_4$ surface absorbed only to carbon species Fig.

6b exhibits the binding energy peaks of ZnWO$_4$ at 1021.4 and 1044.5 eV, which are indicating the Zn 2p3/2 and the Zn 2p1/2 respectively. This confirm the presence of Zn^{2+} ions in the ZnWO$_4$.

3.6 N$_2$ Adsorption–Desorption Isotherms

Fig. 7 presents the N$_2$ adsorption–desorption isotherms of the ZnWO$_4$, WO$_3$–PANI, PANI–ZnWO$_4$ samples to analyze their respective surface area, pore size, and pore volume. The surface areas of the ZnWO$_4$, WO$_3$, WO$_3$–PANI and PANI/ZnWO$_4$/WO$_3$ NCs samples were found to be 194, 214, 264, and 248, m^2/g, respectively. Notably, the introduction of ZnWO$_4$ and WO$_3$ NPs into the PANI matrix enhanced the surface area of the binary nanocomposites, which was further increased for the ternary nanocomposite. The nanostructures can act as spacers increasing the pore size distribution and pore volume of the ternary nanocomposite as determined from Barrett–Joyner–Halenda (BJH) analysis.

* Fig. 7 can be found in the Appendix section.

The pore size and pore volume of the PANI/ZnWO$_4$/WO$_3$ NCs was found to be 5.6 nm and 0.43 cm^3/g, respectively, which were much higher than those of the single nanostructures and binary nanocomposites. Typicaly, the samples exhibit an H$_3$-hysteresis loop suggesting a type-IV isotherm plot. The surface analysis demonstrated about a 28% surface area increase due to the incorporation of the ZnWO$_4$ and WO$_3$. Besides, the "cation–π" and electrostatic interactions established by these compounds considerably affect the pore structure of the ternary nanocomposite. This can provide more adsorption sites and can act as a better charge carrier for light harvesting.

3.7 Band Gap from the UV−vis Absorbance

The band gap can also be estimated from the onset of UV−vis absorbance. Fig 8a shows the UV−vis absorbance divided by film thickness for WO3, 8% Zn/WO$_3$, and ZnWO$_4$ samples of approximately the same thickness (0.20, 0.22, and 0.27 μm, respectively). Using the absorbance data, Tauc plots were created for each of the three samples (Fig. 8b).

* Fig. 8 can be found in the Appendix section.

A Tauc plot can be used to estimate the band gap of a semiconductor because, near the absorption edge, a direct band gap is governed by Eq. 2:

$$(\alpha . h_v)^{1/\gamma}) = B \left(h_v - E_g \right) \tag{2}$$

where; h is the Planck constant, ν is the photon's frequency, Eg is the band gap energy, and B is a constant. The γ factor depends on the nature of the electron transition and is equal to 1/2 or 2 for the direct and indirect transition band gaps, respectively. The band gap energy of PANI/ZnWO$_4$/WO$_3$ NC was calculated as 3.22 eV.

3.8 Cyclic Voltammogram Records

Cyclic voltammogram (CV) records of WO$_3$, PANI and WO$_3$/PANI was detected in 0.7 M LiClO$_4$-PC electrolyte at the scanning rate of 100 mV/s. The inset represents CV of PANI sample. Fig. 9 compares the cyclic voltammetric changes of the films recorded in 0.7 M LiClO$_4$-PC electrolyte in a potential window of -0.8 to 0.6 V, -0.5 to +0.6 V and -1.1 to +0.8 V for WO$_3$, PANI and WO$_3$/PANI films. PANI displayed oxidation peak at approximately +0.6 V in orwarding scan, though the oxidation of aniline was not clearly seen in the forward scan, the reverse scan shows a small shoulder at +0.3 and -0.1 V, which was due to the reduction of PANI formed on the electrode. The WO$_3$ thin film showed a small oxidation and reduction peak at -0.6 and -0.3V vs SCE.

* Fig. 9 can be found in the Appendix section.

However, WO$_3$/PANI film illustrated a large difference among the CV of PANI and WO$_3$. The enhancement of the peak current density of about 0.16 A/cm^2 could be observed in WO$_3$/PANI composite film with respect to pure PANI and WO$_3$ films and is comparable to the earlier reports. This could be due to the anoporous structure of WO$_3$/PANI which provided more reactive centers on the film to contact with the electrolyte and so assist the charge transfer process with improved charge density. This also indicated the catalytic behavior of PANI in WO$_3$. The capacitance from CV curve of all the film calculated using following relation in Eq. 3:

$$C = \frac{I_{max}}{d_s} \tag{3}$$

where, I$_{max}$ is the maximum current (in Ampere) and d$_s$ is the potential scan rate in V/s. Mass of WO$_3$, PANI and WO$_3$/PANI films were measured using a high precision weight balance and is evaluated as 0.0117, 0.0117 and 0.0138 g respectively.

3.9 AC Impedance Spectra (EIS)

AC impedance spectra (EIS) of PANI, WO$_3$, and WO$_3$/PANI were measured to substantiate our approach of injecting PANI over WO$_3$ nanotablets using a hydrothermal method that contributed

superior strength in electricity, ion diffusion process, and structural cyclability]. Fig. 10 displayed the impedance spectra of a WO₃, PANI, and WO₃/PANI measured at +0.38V, +0.07V, and -0.4V respectively.

* Fig. 10 can be found in the Appendix section.

Strikingly, the diffusion layer resistance of WO₃/PANI was lower than their sole performance. An impedance spectrum in the Nyquist plot possesses a straight line inclined by 45° at a higher frequency and a semicircle at a lower frequency. However, the compressed semicircle indicated irregular electrode surface that compensates double layer capacitance by a constant phase element. Particularly, the Nyquist plot of WO₃/PANI exemplified small straight line at higher frequencies as a result of the diffusion process and a broad semicircle in the smaller frequency attributed to fast electron transfer and its prolonged existence in the film.

3.10 Galvanostatic Charge/Discharge Curves

The galvanostatic charge-discharge is a trustworthy technique to measure the electrochemical behavior of the material under controlled conditions using three electrode systems with 0.5 M LiClO₄-PC electrolyte. Fig. 11(a) exhibited charge/discharge curves of PANI, WO₃, and WO₃/PANI for initial cycles at constant current density of 0.05, 0.5 and 0.05 mA/cm² respectively, while Fig. 11(b) represents charge-discharge cycles for initial 10 cycles of WO₃/PANI films.

* Fig. 11 can be found in the Appendix section.

The potential responses of the composite film during charge-discharge were more symmetrical than the sole performance of WO₃ and the working potential could be extended to 0.8 V. The discharge curve represented the characteristic profile of a pseudocapacitance showing the potential dependent nature of faradic reaction. When we correlated charge/discharge with the morphological study, it indicated that WO₃ has a larger particle size that decreases surface density increasing the interplanar spacing between atoms. Thus, during the charging process, it utilizes less coulombic force that accumulates large charges in a short time. Subsequently, the capacity of WO₃ increases with less charge-discharge time n PANI, the charge-discharge time increases because it is highly conductive consisting of many electrons that enhances displacement of the electron cloud. Accordingly, it utilizes more coulombic force with the increase in charge-discharge time. However,

when PANI coated over WO₃, it enhances the surface area of WO₃ with the reduction in the distance. Ultimately the resistance decreases intrinsically with the improved charge transport process. Owing to this, WO₃/PANI uses more coulombic force with more time for charging and discharging process. Therefore, the charge storing capacity of the system enhances. The capacitance from charge/discharge curves evaluated using following relation in Eq. 4:

$$C = \frac{Itd}{M\delta v} \qquad (4)$$

where; I and td are the in applied current density and time discharge, ΔV is the potential range, m is the mass of deposited film mentioned above.

3.11 The Effect of Increasing PANI/ZnWO₄/WO₃ NCs Concentrations on GLP and HZN Removals

Maximum 99% GLP removal was observed at 1.0 mg/l PANI/ZnWO₄/WO₃ NCs, after 180 min photodegradation, under 300 W solar light at pH=7.0 and at a temperature of 25 °C (Table 2). The cost of a nanocomposite in practical application depends to a large extent on its specific dosage to achieve the wastewater treatment standards. In this work, the correlation of the NCs dosage and the removal efficiency of GLP was explored. It can be clearly observed that the removal efficiency of GLP increases from about 68% to almost 99% as the PANI/ZnWO₄/WO₃ NCs dosage increases from 0.1 to 1.5 mg/l. However, there is no evident growth anymore when the dosage exceeds 1.5 mg/l. The reason for this might be that more available binding sites are provided to capture GLP molecules in solution with the increased content of the nanocomposite. To reduce the expense of GLP disposal, an optimal PANI/ZnWO₄/WO₃ NCs dosage of 1 mg/l is suggested for the efficient elimination of GLP.

* Table 2 can be found in the Appendix section.

The maximum HZN removal was 96% at 1.0 mg/l PANI/ZnWO₄/WO₃ NCs, after 180 min photodegradation, under 300 W solar lights at pH=7.0 and at a temperature of 25°C (data not shown). A significant linear correlation between nanocomposite concentration and herbicide yields was observed up to a nanocomposite concentration of 15 mg/l ($r^2 = 0.91$, p = 0.07, F = 0.76). ANOVA test indicated that there were significant differences between nanocomposite concentration and herbicide

removals for PANI/ZnWO₄/WO₃ NCs concentration > 1.00 (p = 1.87, F =9.14, d.f. = 2).

3.12 The Effect of Different PANI/ZnWO₄/WO₃ Mass Ratios on GLP and HZN Removals

Maximum 99% GLP removal was measured at 1:2:3 mass ratio of PANI to ZnWO and to /WO₃ NCs after 180 min photodegradation, under 300 W solar light, at pH=7.0 and and at 25°C temperature (Table 3). It could be seen from this table that the increase in ZnWO₄ and WO₃ percentages in the whole NCs resulted in an increase from 68 to 99.7% in the photooxidation yields of GLPs(V). This may be due to the greater availability of the exchangeable sites or surface area at higher concentrations of the ZnWO₄ and WO₃ percentages.

* Table 3 can be found in the Appendix section.

The Maximum HZN removal yield was 95% at 1:2:3 mass ratio of PANI/ZnWO₄/WO₃ NCs after 180 min photodegradation, under 300 W solar lights, at pH=7.0 and and at 25°C temperature (data not shown). A significant linear correlation between mass ratio of PANI to ZnWO and to WO₃ in the nanocomposite and herbicide yields was observed up to a mass ratio of 3:1:1 and 3:2:1 (r^2 = 0.91, p = 0.07, F = 0.76). ANOVA test indicated that there were significant differences between mass ratio of PANI to ZnWO₄ and to /WO3 and herbicide yields at ratios > 1:2:3 (p = 1.87, F =9.14, d.f. = 2).

3.13 The Effect of Different GLP and HZN Concentrations on GLP and HZN Removals

Maximum 99% GLP removal was found at 3 mg/l GLP, after 180 min photodegradation, under 300 W solar lights at pH=7.0 and at 25 °C (Table 4). An increase in the GLP concentration from 1 mg/l up to 4 mg/l increased the photodegradation yields of GLP. This may be due to the almost all GLP photocatalyzed by PANI/ZnWO₄/WO₃ NCs and the establishment of equilibrium between the NCs and GLP and none of a GLP photocatalyst was not remained in the solution. At 3 mg/l GLP more NCs surface or more adsorption spots were available for the solute to be photocatalyzed. A further increase in photocatalyst dosage (4 mg/l) did not cause a significant improvement in GLP adsorption. This may be due to the adsorption of almost all GLP to the photocatalyst and the establishment of equilibrium between the GLP adsorbed to the NCs and those remaining unabsorbed and unphotocatalyzed in the solution. The loading amount of catalyst is a

significant factor in the photocatalytic degradation process, because the efficiency could be strongly affected by the number of active sites and photo-adsorption ability of the catalyst used. However, it was observed that above a certain optimum catalyst mass, the reaction rate decreases and becomes independent of the catalyst concentration.

* Table 4 can be found in the Appendix section.

The maximum HZN removals was 96% at 3 mg/l GLP, after 180 min photodegradation, under 300 W solar light at pH=7.0 and at 25°C (data not shown). A significant linear correlation between GLP and HZN concentrations and herbicide yields was observed up to a nanocomposite concentration of 4 mg/l (r^2 = 0.91, p = 0.07, F = 0.76). ANOVA test indicated that there were significant differences between nanocomposite concentration and herbicide removals for PANI/ZnWO₄/WO₃ NC concentration > 4.00 mg/l (p = 1.87, F =9.14, d.f. = 2).

3.14 The Effect of Increasing Photodegradation Time on GLP and HZN Removals

Maximum 99% GLP removal was obtained after 15 min photodegradation, under 300 W solar lights, at pH=7.0 and at 25°C (Table 5). As the photooxidation times were increased from 2 min up to 15 min the GLP yields increased from 68% up to 99% under sun light. Further increase of time did not affect the GLP removals. Data obtained from this study showed that the GLP yields at longer retention time was low. In an elevated ratio of contact at long contact times; no hydroxyl radicals production was achieved for GLR reduction. As a result, low conversion rates were observed at shorter residence times. The optimum illumination time for maximum removal of GLP was obtained as 15 min.

* Table 5 can be found in the Appendix section.

The maximum HZN removal was obtained as 97% after 15 min photodegradation, under 300 W solar light, at pH=7.0 and at 25°C (data not shown). A significant linear correlation between photodegradation time and herbicide yields was observed up to a time of 20 min (r^2 = 0.91, p = 0.07, F = 0.76). ANOVA test indicated that there were significant differences between photodegradation time and herbicide removals for time > 15 min (p = 1.87, F =9.14, d.f. = 2).

3.15 The Effect of Increasing Solar Light Power on GLP and HZN Removals

Maximum 99% GLP removal was measured at 80 W/m^2 solar light power after 180 min photodegradation, under 300 W solar lights at pH=7.0 and at 25°C (Table 6). Photocatalytic reaction rate depends largely on the radiation absorption of the photocatalyst, where the increase in light intensity enhances the degradation rate and the yield in photocatalytic degradation. At low light intensities (20–60 W/m^2), the rate would increase linearly with increasing light intensity, whereas at intermediate light intensities, above 14 W/m^2, the rate would depend on the square root of the light intensity. This is likely, because at low light intensity, reactions involving electron–hole formation are predominant, and electron–hole recombination is negligible. However, at increased light intensity, electron–hole pair separation competes with recombination, thereby causing lower effect on the reaction rate like a solar light power of 100 W/m^2. The enhancement of the photodegradation of GLP increased as the light intensity increased up to 100 W/m^2.

* Table 6 can be found in the Appendix section.

Maximum 96% HZN removal was measured at 80 W/m^2 solar light power after 180 min photodegradation, under 300 W solar lights at pH=7.0 and at 25°C (data not shown). A significant linear correlation between sunligth power and herbicide yields was observed up to a sunligth power of 350 W/m^2 (r2 = 0.91, p = 0.07, F = 0.76). ANOVA test indicated that there were significant differences between sunligth power and herbicide removals for sun ligth power > 300 W/m^2 (p = 1.87, F =9.14, d.f. = 2).

3.16 Acute Toxicity Assays
3.16.1 Effect of Increasing GLP and HZN Concentrations on the Microtox Acute Toxicity at Increasing Photocatalytic Degradation Time and Temperature

It was found a high toxicity in raw surface water based on Microtox bacteria (Aliivibrio fischeri also called *Vibrio fischeri*). In Microtox with *Aliivibrio fischeri* acute toxicity test, the initial EC_{90} =825 mg/l was found at pH=7.0, at 25°C (Table 7: SET 1). The EC_{90} values decreased to EC_{57}=414 mg/l to EC_{22}=236 mg/l and to EC_{12}=165 mg/l at GLP=3 mg/l, after 60, 120 and 180 min photocatalytic degradation time, at 30°C (Table 7: SET 3). The Microtox acute toxicity removal efficiencies were 40.86%, 79.75% and 90.86% after 60, 120 and 180 min photocatalytic

degradation time, respectively, at GLP=3 mg/l, and a temperature of 30°C (Table 7: SET 3).

* Table 7 can be found in the Appendix section.

The EC_{90} values decreased to EC_{51}=550 mg/l, EC_{17}=214 mg/l and EC_7=5 mg/l after 60, 120 and 180 min photocatalytic degradation time, respectively, at GLP=3 mg/l at 60°C (Table 7: SET 3). The toxicity removal efficiencies were 46.41%, 85.30% and 96.41% after 60, 120 and 180 min photocatalytic degradation time, respectively, at GLP=3 mg/l, and a temperature of 60°C (Table 7: SET 3). 96.41% maximum Microtox acute toxicity removal was found in GLP=3 mg/l after 180 min photocatalytic degradation time, at 60°C (Table 7: SET 3).

The EC_{90} values decreased to EC_{62}=422 mg/l, to EC_{21}=241 mg/l and to EC_{17}=168 mg/l after 60, 120 and 180 min photocatalytic degradation time, respectively, at GLP=1 mg/l at 30°C (Table 7: SET 3). The EC_{90} values decreased to EC_{62}=421 mg/l, to EC_{27}=239 mg/l and to EC_{11}=167 mg/l after 60, 120 and 180 min photocatalytic degradation time, respectively, at GLP=2 mg/l at 30°C. The EC_{90} values decreased to EC_{67}=408 mg/l, to EC_{32}=230 mg/l and to EC_{22}=162 mg/l after 60, 120 and 180 min photocatalytic degradation time, respectively, at GLP=4 mg/l at 30°C. The Microtox acute toxicity removals were 85.30%, 85.28% and 79.75% in 1 mg/l, 2 mg/l and 4 mg/l GLP, respectively, after 180 min photocatalytic degradation time, at 30°C. It was obtained an inhibition effect of GLP=4 mg/l to *Vibrio fischeri* after 180 min photocatalytic degradation time, at 30°C (Table 7: SET 3).

The EC_{90} values decreased to EC_{57}=419 mg/l, to EC_{22}=266 mg/l and to EC_{12}=150 mg/l after 60, 120 and 180 min photocatalytic degradation time, respectively, at GLP=1 mg/l at 60°C (Table 7: SET 3). The EC_{90} values decreased to EC_{57}=414 mg/l, to EC_{22}=232 mg/l and to EC_{12}=161 mg/l after 60, 120 and 180 min photocatalytic degradation time, respectively, in GLP=2 mg/l, at 60°C. The EC_{90} values decreased to EC_{62}=403 mg/l, to EC_{27}=218 mg/l and to EC_{17}=148 mg/l after 60, 120 and 180 min photocatalytic degradation time, respectively, in GLP=4 mg/l at 60°C. The Microtox acute toxicity removals were 90.86%, 90.83% and 85.30% in 1 mg/l, 2 mg/l and 4 mg/l GLP, respectively, after 180 min photocatalytic degradation time, at 60°C. It was observed an inhibition effect of GLP=4 mg/l to *Vibrio fischeri* after 180 min photocatalytic degradation time, at 60°C (Table 7: SET 3). The Microtox acute toxicity removals were 88.80%, 86.83% and 80.38% in 1 mg/l, 2 mg/l and 4 mg/l

HZN, respectively, after 180 min photocatalytic degradation time, at 60ºC (data not shown).

3.16.2 Effect of Increasing GLP and HZN Concentrations on the *Daphnia magna* Acute Toxicity at Increasing Photocatalytic Degradation Time and Temperature in the Raw Surface Water

A high toxicity was found for raw surface water before photooxidation in the acute toxicity tests performed by *Daphnia magna*. The initial $EC_{50}=850$ mg/l was observed at 25ºC (Table 8: SET 1). After 60, 120 and 180 min photocatalytic degradation time, the EC_{50} values decreased to $EC_{31}=350$ mg/l, to $EC_{17}=240$ mg/l and to $EC_{12}=90$ mg/l in GLP=3 mg/l, at 30ºC (Table 8: SET 3). The *Daphnia magna acute* toxicity removals were 42.96%, 72.87% and 82.65% after 60, 120 and 180 min photocatalytic degradation time, respectively, in GLP=3 mg/l, at 30ºC (Table 8: SET 3).

* Table 8 can be found in the Appendix section.

The EC_{50} values decreased to $EC_{27}=150$ mg/l, to $EC_{12}=60$ mg/l and to $EC_{7}=6$ mg/l after 60, 120 and 180 min photocatalytic degradation time, respectively, in GLP=3 mg/l, at 60ºC (Table 8: SET 3). The toxicity removal efficiencies were 52.94%, 82.62% and 92.36% after 60, 120 and 180 min photocatalytic degradation time, respectively, in GLP=3 mg/l, at 60ºC (Table 8: SET 3). 92.38% maximum *Daphnia magna* acute toxicity removal was obtained in GLP=3 mg/l after 180 min photocatalytic degradation time, at 60ºC, respectively (Table 8: SET 3).

The EC_{50} values decreased to $EC_{37}=450$ mg/l, to $EC_{22}=145$ mg/l and to $EC_{17}=260$ mg/l after 60, 120 and 180 min photocatalytic degradation time, respectively, in GLP=1 mg/l at 30ºC (Table 8: SET 3). The EC_{50} values decreased to $EC_{37}=450$ mg/l, to $EC_{22}=175$ mg/l and to $EC_{17}=100$ mg/l after 60, 120 and 180 min photocatalytic degradation time, respectively, in GLP=2 mg/l and at 30ºC. The EC_{50} values decreased to $EC_{42}=300$ mg/l, to $EC_{27}=170$ mg/l and to $EC_{22}=52$ mg/l after 60, 120 and 180 min photocatalytic degradation time, respectively, in GLP=4 mg/l, at 30ºC. The *Daphnia magna* acute toxicity removals were 72.22%, 72.56% and 63.21% in 1 mg/l, 2 mg/l and 4 mg/l GLP, respectively, after 180 min photocatalytic degradation time, at 30ºC. It was observed an inhibition effect of GLP=4 mg/l to *Daphnia magna* after 180 min photocatalytic degradation time, at 30ºC (Table 8: SET 3).

The EC_{50} values decreased to $EC_{32}=130$ mg/l, to $EC_{17}=425$ mg/l and to $EC_{12}=340$ mg/l after 60, 120 and 180 min photocatalytic degradation time, respectively, in GLP=1 mg/l, at 60ºC (Table 8: SET 3). The EC_{50} values decreased to $EC_{32}=425$ mg/l, to $EC_{17}=140$ mg/l and to $EC_{7}=90$ mg/l after 60, 120 and 180 min photocatalytic degradation time, respectively, in GLP=2 mg/l, at 60ºC. The EC_{50} values decreased to $EC_{37}=250$ mg/l, to $EC_{22}=110$ mg/l and to $EC_{17}=10$ mg/l after 60, 120 and 180 min photocatalytic degradation time, respectively, in GLP=4 mg/l, at 60ºC. The *Daphnia magna* acute toxicity removals were 83.06%, 92.65% and 73.11% in 1 mg/l, 2 mg/l and 4 mg/l GLP, respectively, after 180 min photocatalytic degradation time, at 60ºC. It was observed an inhibition effect of GLP=4 mg/l to *Daphnia magna* after 180 min photocatalytic degradation time, at 60ºC (Table 8: SET 3).

Increasing the GLP concentrations from 1 mg/l to 3 mg/l did not have a positive effect on the decrease of EC_{50} values as shown in Table 8 at SET 3. GLP concentrations > 3 mg/l decreased the acute toxicity removals by hindering the photocatalytic degradation process. Similarly, a significant contribution of increasing GLP concentration to acute toxicity removal at 60ºC after 180 min photocatalytic degradation time was not observed. Low toxicity removals found at high GLP concentrations could be attributed to their detrimental effect on the *Daphnia magna* (Table 8: SET 3)*. The *Daphnia magna* acute toxicity removals were 78.09%, 88.60% and 70.14% in 1 mg/l, 2 mg/l and 4 mg/l HZN, respectively (data not shown).

3.17 Aplication of PANI/ZnWO₄/WO₃ NCs to the Surface Water which is Going to be Used as Drinking Water

Water treatment and purification in environmental protection are the worldwide issues to relieve the water shortage. At present, various treatment technologies for drinking water or wastewater have been developed. Firstly, the purification processes for drinking water are introduced including the efficiency and mechanism of filtration and sedimentation, flocculation and disinfection. In order to remove the GLP and HZN herbicides with maximum yields of 99% and 96%, respectively, 3 mg PANI/ZnWO₄/WO₃ NCs should be added to 1 liter of surface water to the sedimentation tank of the drinking water treatment process. The retention time should be 180 min, at 300 W solar light at pH=7.0 and at 25 ºC.

Rukiye Öztekin, Delia Teresa Sponza

4 Conclusion

PANI/ZnWO$_4$/WO$_3$ NCs was produced under laboratory conditions to remove GLP and HZN herbicides from the surface water via photooxidation. In order to detect the maximum GLP and HZN photodegradation yields for optimum operational conditions (the effects of increasing PANI/ZnWO$_4$/WO$_3$ NCs concentrations, PANI/ZnWO$_4$/WO$_3$ mass ratios, GLP and HZN concentrations, photocatalytic degradation times and solar light powers on GLP and HZN removals) was investigated. The maximum removal conditions for GLP (99.90%) and HZN (96.00%) were 3 mg/l PANI/ZnWO$_4$/WO$_3$ NCs with a mass ratio of 1:2:3 of PANI to ZnWO$_4$ and to WO$_3$, after 15 min photocatalytic degradation time at 80 W/m^2 power, at 25°C.

The toxicity of raw and photodegraded surface water was examined using Microtox (with *Aliivibrio fischeri*) and *Daphnia magna* acute toxicity tests. The acute toxicity decreased significantly in photodegraded surface water. The acute toxicity analysis showed that the surface water was toxic and the toxicity decreased after photocatalytic treatment. PANI/ZnWO$_4$/WO$_3$ NCs exhibited slightly toxicity after a concentration of 5 mg/l and 6 mg/l for Microthox and *Daphnia magna* acute toxicity, respectively.

The crystalline structure of monoclinic ZnWO$_4$ and WO$_3$ was detected from XRD analysis while PANI exhibited a broad characteristic maximum peak at 28.91° with an amorphous structure. FTIR spectra showed that pure ZnWO$_4$ has the Zn–O–W vibrational bands. For WO$_3$ nanostructures, the vibrational band at 740 cm^{-1} represent the presence of W–O–W stretching while PANI was observed at 850 cm^{-1} describing the C/-C vibrational mode of the quinoid and benzenoid rings. Therefore, in the XPS the radical trapping and ROS quantification (OH$^{•}$ and O$_2^{·-•}$) analysis explained the double electron transfer type of Z-scheme mechanism ending with the cleavage of N–C bonds in the GLP and HZN herbicides. The survey spectra of PANI, ZnWO$_4$ NPs, WO$_3$ NPs and PANI/ZnWO$_4$/WO$_3$ NCs, which displays four peaks at 410 eV, 397 eV, 398.9 eV, and 399 eV, shows the existence of W, Zn, O, and C elements. Pristine ZnWO$_4$ shows the adsorption of carbon species by ZnWO$_4$ surface.

A novel, efficient, and non-toxic PANI/ZnWO$_4$/WO$_3$ NCs, synthesized following an IL-assisted in situ oxidative polymerization method. The prepared nanocomposite was utilized towards improved photocatalytic wastewater treatment and acute toxicity removal. Comprehensive analysis of the structural and morphological properties of the nanocomposite revealed high structural integrity and close contact between the individual components.

Very high photocatalytic degradation efficiencies were obtained with the effect of sunlight irradiation in the use of PANI/ZnWO$_4$/WO$_3$ NCs to remove the GLP and HZN herbicides from surface water. PANI/ZNWO$_4$/WO$_3$ NCs are non-toxic, costly-effective, easy to apply and can be successfully applied in the removal of different toxic and refractory pollutants from surface waters.

Abbreviations
Al: Aluminum
(NH$_4$)$_2$S$_2$O$_8$: Ammonium persulfate
AMPA: Aminomethylphosphonic acid
AOPs: Advanced oxidation processes
ATSDR: Agency for Toxic Substances and Disease Registry
BiOBr: Bismuth oxobromide
BiVO$_4$: Bismuth vanadate
Bi$_2$WO$_6$: Bismuth tungstate
C: Carbon
C$_o$: the pollutant concentration before illumination
CDC: the Centers for Disease Control and Prevention
Ce: Cerium
CO$_2$: Carbon dioxide
C$_t$: the final concentration of the pollutant at time t.
C$_2$H$_3$N: Acetonitrile
Cu: Copper
Cu(OH)$_2$: Copper hydroxide
CV: Cyclic voltammogram
DIN: "Deutsches Institut für Normung", meaning "German institute for standardization"
DO: Dissolved oxygen
D201Cu: Nanosized copper hydroxide modified resin
EC: Effective concentration in toxicity measurement
EC$_{50}$: 50% Effective concentration in toxicity measurement
Fe$_3$O$_4$: Iron (II, III) oxide or Magnetite
FESEM: Field emission scanning electron microscopy
FMOC: 9-fluorenylmethyl chloroformate
FTIR: Fourier transform infrared spectroscopy
GC-MS: Gas Chromatography Mass Spectrometry
GLP: Glyphosate
g-C$_3$N$_4$: Graphitic carbon nitride
He: Helium
H$_2$O: Water
H$_2$O$_2$: Hydrogen peroxide
H$_2$SO$_4$: Sulfuric acid
HAc: Acetic acid
HCl: Hydrogen chloride

HRTEM: High resolution transmission electron microscopy
IARC: International Agency for Research on Cancer
IR: Infrared
La: Lanthanum
MB: Methylene blue
Mn: Manganese
$MnFe_2O_4$: Manganese iron oxide
MnO_2: Manganese dioxide
MPA: Methylphosphonic acid
MSD: Mass selective detector
NaOH: Sodium hydroxide
NBT: Nitro blue tetrazolium dichloride
NCs: Nanocomposites
NH_4Ac: Ammonium ethanoate
NPs: Nanoparticles
O: Oxygen
O^{2-}: Oxygen ion
$O_2^{-\bullet}$: Superoxide radicals
$OH^\bullet$: hydroxyl radicals
PANI: Polyaniline
PO_4-P: Orthophosphate
ROS: Reactive oxygen species
SD: Standard deviation
TiO_2: Titanium dioxide
US: United States
UV: Ultraviolet
W: Tungsten
WO_3: Tungsten trioxide
WO_4: Wolframite
WO_6: Trioxido-oxo-tungsten
XPS: X-Ray photoelectron spectroscopy
XRD: X-Ray diffraction
Zn: Zinc
Zn^{2+}: Zinc ions
ZnO: Zinc oxide
$ZnWO_4$: Zinc tungsten oxide or Zinc tungstate

References:
[1] P.R. Rout, T.C. Zhang, P. Bhunia, P.Y. Surampalli, Treatment Technologies for Emerging Contaminants in Wastewater Treatment Plants: A Review, *Science of the Total Environment*, Vol.753, 2021, 141990.

[2] B. Song, P. Xu, M. Chen, W. Tang, G. Zeng, J. Gong, P. Zhang, S. Ye, Using Nanomaterials to Facilitate the Phytoremediation of Contaminated Soil, *Critical Reviews in Environmental Science and Technology*, Vol.49, No.9, 2019, pp. 791–824.

[3] H. Xiang, Y. Zhang, D. Atkinson, R. Sekar, Effects of Anthropogenic Subsidy and Glyphosate on Macroinvertebrates in Streams, *Environmental Science and Pollution Research*, Vol.27, No.17, 2020, pp. 21939–21952.

[4] C.R. García-García, T. Parrón, M. Requena, R. Alarcón, A.M. Tsatsakis, A.F. Hernández, Occupational Pesticide Exposure and Adverse Health Effects at the Clinical, Hematological and Biochemical Level, *Life Sciences*, Vol.145, 2016, pp. 274–283.

[5] I.A. Saleh, N. Zouari, M.A. Al-Ghouti, Removal of Pesticides from Water and Wastewater: Chemical, Physical and Biological Treatment Approaches, *Environmental Technology & Innovation*, Vol.19, 2020, 101026.

[6] A. Sharma, V. Kumar, B. Shahzad, M. Tanveer, G.P.S. Sidhu, N. Handa, S.K. Kohli, P. Yadav, A.S. Bali, R.D. Parihar, O.I. Dar, K. Singh, S. Jasrotia, P. Bakshi, M. Ramakrishnan, S. Kumar, R. Bhardwaj, A.K. Thukral, Worldwide Pesticide Usage and its Impacts on Ecosystem, *SN Applied Sciences*, Vol.11, No.1, 2019, pp. 1446-1462.

[7] S. Mostafalou, M. Abdollahi, Pesticides and Human Chronic Diseases: Evidences, Mechanisms, and Perspectives, *Toxicology and Applied Pharmacology*, Vol.268, No.2, 2013, pp. 157–177.

[8] J.E. Casida, K.A. Durkin, Pesticide Chemical Research in Toxicology: Lessons from Nature, *Chemical Research in Toxicology*, Vol.30, 2017, pp. 94–104.

[9] M. Abdennouri, M. Baâlala, A. Galadi, M. El Makhfouk, M. Bensitel, K. Nohair, M. Sadiq, A. Boussaoud, N. Barka, Photocatalytic Degradation of Pesticides by Titanium Dioxide and Titanium Pillared Purified Clays, *Arabian Journal of Chemistry*, Vol.9, 2016, pp. S313–S318.

[10] G. Liu, L. Li, X. Huang, S. Zheng, X. Xu, Z. Liu, Y. Zhang, J.D. Wang, D. Xu, Adsorption and Removal of Organophosphorus Pesticides from Environmental Water and Soil Samples by Using Magnetic Multi-Walled Carbon Nanotubes@ Organic Framework ZIF-8, *Journal of Materials Science*, Vol.53, No.15, 2018, pp. 10772–10783.

[11] R. Pandiselvam, R. Kaavya, Y. Jayanath, K. Veenuttranon, P. Lueprasitsakul, V. Divya, A. Kothakota, S.V. Ramesh, Ozone as a Novel Emerging Technology for the Dissipation of

Pesticide Residues in Foods—A Review, *Trends in Food Science & Technology*, Vol.97, 2020, pp. 38–54.

[12] N. Barka, S. Qourzal, A. Assabbane, A. Nounah, Y. Ait-Ichou, Photocatalytic Degradation of an Azo Reactive Dye, Reactive Yellow 84, in Water Using an Industrial Titanium Dioxide Coated Media, *Arabian Journal of Chemistry*, Vol.3, No.4, 2010, pp. 279–283.

[13] M.H. Dehghani, Y. Karamitabar, F. Changani, Z. Heidarinejad, High Performance Degradation of Phenol from Aqueous Media Using Ozonation Process and Zinc Oxide Nanoparticles as a Semiconductor Photo Catalyst in the Presence of Ultraviolet Radiation, *Desalination and Water Treatment*, Vol.166, 2019, pp. 105–114.

[14] A.O. Ibhadon, P. Fitzpatrick, Heterogeneous Photocatalysis: Recent Advances and Applications, *Catalysts*, Vol.3, No.1, 2013, pp. 189–218.

[15] W.L. Silva, M.A. Lansarin, P.R. Livotto, J.H.Z. Santos, Photocatalytic Degradation of Drugs by Supported Titania-Based Catalysts Produced from Petrochemical Plant Residue, *Powder Technology*, Vol.279, 2015, pp. 166–172.

[16] R.S. Dariani, A. Esmaeili, A. Mortezaali, S. Dehghanpour, Photocatalytic Reaction and Degradation of Methylene Blue on TiO_2 Nano-Sized Particles, *Optik-International Journal for Light and Electron Optics*, Vol.127, 2016, pp. 7143–7154.

[17] P.V. Kamat, TiO_2 Nanostructures: Recent Physical Chemistry Advances, *The Journal of Physical Chemistry C: Nanomaterials and Interfaces*, Vol.116, No.22, 2012, pp. 11849–11851.

[18] S. Hernández, D. Hidalgo, A. Sacco, A. Chiodoni, A. Lamberti, V. Cauda, E. Tresso, G. Saracco, Comparison of Photocatalytic and Transport Properties of TiO_2 and ZnO Nanostructures for Solar-Driven Water Splitting, *Physical Chemistry Chemical Physics*, Vol.17, 2015, pp. 7775–7786.

[19] M. Yoldi, E. Fuentes-Ordoñez, S. Korili, A. Gil, Zeolite Synthesis from Industrial Wastes, *Microporous and Mesoporous Materials*, Vol.287, 2019, pp. 183–191.

[20] S. Mintova, M. Jaber, V. Valtchev, Nanosized Microporous Crystals: Emerging Applications, *Chemical Society Reviews*, Vol.44, 2015, pp. 7207–7233.

[21] G. Williams, R. Kroes, I. Munro, Safety Evaluation and Risk Assessment of the Herbicide Roundup and its Active Ingredient, Glyphosate, For Humans, *Regulatory Toxicology and Pharmacology*, Vol.31, No.2 Pt 1, 2000, pp. 117–165.

[22] C. Benbrook, Trends in Glyphosate Herbicide Use in the United States and Globally, *Environmental Sciences Europe*, Vol.28, No.1, 2016, Article number:3.

[23] Y. Huang, Z. Li, K. Yao, C. Chen, C. Deng, Y. Fang, R. Li, H. Tian, Supressing Toxic Intermediates During Photocatalytic Degradation of Glyphosate by Controlling Adsorption Modes, *Applied Catalysis B: Environment and Energy*, Vol.299, 2021, 120671.

[24] ATSDR, *Toxicological Profile for Silica*, Atlanta, GA, U.S. Department of Health and Human Services, Public Health Service, United States, 2019.

[25] CDC, *Fourth National Report on Human Exposure to Environmental Chemicals*, Atlanta (GA), United States, 2019.

[26] B.J. Simoneaux, T.J. Gould, Chapter 7 - Plant Uptake and Metabolism of Triazine Herbicides, *The Triazine Herbicides: 50 years Revolutionizing Agriculture*, 2008, pp. 73-99.

[27] A.F. Méndez –Villaquiran, *Aislamiento e Identificación de Bacterias Capaces de Degradar Glifosato*, Universidad ICESI, Facultad de Ciencias Naturales, Departamento Ciencias Química - Programa Química Farmacéutica, Santiago de Cali – Colombia, 2015.

[28] M. Wang, G. Zhang, G. Qiu, D. Cai, Z. Wu, Degradation of Herbicide (Glyphosate) Using Sunlight-Sensitive MnO_2/C Catalyst Immediately Fabricated by High Energy Electron Beam, *Journal of Chemical Engineering*, Vol.306, 2016, pp. 693-703.

[29] U. Ahrens, E. Seemüller, Detection of Mycoplasmalike Organisms in Declining Oaks by Polymerase Chain Reaction, *European Journal of Forest Pathology*, Vol.24, No.1, 1994, pp. 55-63.

[30] X. Cao, C. Xu, X. Liang, J. Ma, M. Yue, Y. Ding, Rationaly Designed/Assembled Hybrid $BiVO_4$-Based Photoanode for Enhanced Photoelectrochemical Performance, *Applied Catalysis B: Environment and Energy*, Vol.260, 2020, 118136.

[31] Y. Yang, Q. Deng, W: Yan, C. Jing, Y. Zhang, Comparative Study of Glyphosate Removal on Goethite and Magnetite: Adsorption and Photo-Degradation, *Chemical Engineering Journal*, Vol.352, 2018, pp. 581-589.

[32] C. Zhou, D. Jia, M. Liu, X. Liu, C. Li, Removal of Glyphosate from Aqueous Solution Using Nanosized Copper Hydroxide Modified Resin: Equilibrium Isotherms and Kinetics, *Journal of Chemical & Engineering Data*, Vol.62, No.10, 2017, pp. 3585–3592.

[33] M. Mei, Z. Du, R. Xu, Y. Chen, H. Zhang, S. Qu, Photocatalytic Degradation of Hexazinone and Its Determination in Water via UPLC–MS/MS, *Journal of Hazardous Materials*, Vol.221–222, 2012, pp. 100-108.

[34] T. Jasemizad, L.P. Padhy, Photodegradation and Adsorption of Hexazinone (HZN) in Aqueous Solutions: Removal Efficiencies, Kinetics, and Mechanisms, *Environmental Science and Pollution Research*, Vol.29, 2022, pp. 48330–48339.

[35] Y. Yao, M. Li, Y. Yang, L. Cui, L. Guo, Electrochemical Degradation of Insecticide Hexazinone with Bi-doped PbO_2 Electrode: Influencing Factors, Intermediates and Degradation Mechanism, *Chemosphere*, Vol.216, 2019, pp. 812-822.

[36] Y. Okamoto, W. Brenner, *Organic Semiconductors*, New York: Reinhold Publishing Corporation, United States, 1964.

[37] A. Heeger, Nobel Lecture: Semiconducting and Metallic Polymers: The Fourth Generation of Polymeric Materials, *Reviews of Modern Physics*, Vol.73, No.3, 2001, pp. 681–700.

[38] S. Chen, D. Huang, G. Zeng, W. Xue, L. Lei, P. Xu, R. Deng, J. Li, M. Cheng, In-situ Synthesis of Facet-Dependent $BiVO_4$/Ag_3PO_4/PANI Photocatalyst with Enhanced Visible-Light-Induced Photocatalytic Degradation Performance: Synergism of Interfacial Coupling and Hole-Transfer, *Chemical Engineering Journal*, Vol.382, 2020, 122840.

[39] J. Jiang, H. Li, L. Zhang, New Insight into Daylight Photocatalysis of AgBr@Ag: Synergistic Effect Between Semiconductor Photocatalysis and Plasmonic Photocatalysis, *European Journal of Chemistry*, Vol.18, No.20, 2012, pp. 6360–6369.

[40] C.V. Reddy, R. Koutavarapu, I.N. Reddy, J. Shim, Effect of a Novel One-Dimensional Zinc Tungsten Oxide Nanorods Anchored Two-Dimensional Graphitic Carbon Nitride Nanosheets for Improved Solar-Light-Driven Photocatalytic Removal of Toxic Pollutants and Photoelectrochemical Water Splitting, *Journal of Materials Science: Materials in Electronics*, Vol.32, 2021, pp. 33–46.

[41] J. Ke, M.A. Younis, Y. Kong, H. Zhou, J. Liu, L. Lei, Y. Hou, Nanostructured Ternary Metal Tungstate-Based Photocatalysts for Environmental Purification and Solar Water Splitting: A Review, *Nano-Micro Letters*, Vol.10, 2018, Article number:69.

[42] D.P. Ojha, H.J. Kim, Investigation of Photocatalytic Activity of ZnO Promoted Hydrothermally Synthesized ZnWO4 Nanorods in UV–Visible Light Irradiation, *Chemical Engineering Science*, Vol.212, 2020, 115338.

[43] G. He, H. Fan, L. Ma, K. Wang, D. Ding, C. Liu, Z. Wang, Synthesis, Characterization and Optical Properties of Nanostructured $ZnWO_4$, *Materials Science in Semiconductor Processing*, Vol.41, 2016, pp. 404–410.

[44] G. Chen, F. Wang, J. Yu, H. Zhang, X. Zhang, Improved Red Emission by Codoping Li^{+3} in $ZnWO_4$:Eu^{+3} Phosphors, *Journal of Molecular Structure*, Vol.1128, 2017, pp. 1–4.

[45] A.F. Gouveia, M. Assis, L.S. Cavalcante, L. Gracia, E. Longo, J. Andres, Reading at Exposed Surfaces: Theoretical Insights into Photocatalytic Activity of $ZnWO_4$, *Frontier Research Today*, Vol.1, 2018, 1005.

[46] B. Zhai, L. Yang, Y. Huang, Intrinsic Defect Engineering in Eu^{+3} Doped $ZnWO_4$ for Annealing Temperature Tunable Photoluminescence, *Nanomaterials*, Vol.9, No.1, 2019, 99.

[47] S. Wei, Y. Ma, Y. Chen, L. Liu, Y. Liu, Z. Shao, Fabrication of WO_3/Cu_2O Composite Films and Their Photocatalytic Activity, *Journal of Hazardous Materials*, Vol.194, 2011, pp. 243–249.

[48] F. Wang, C. Di Valentin, G. Pacchioni, Rational Band Gap Engineering of WO_3 Photocatalyst for Visible Light Water Splitting, *ChemCatChem*, Vol.4, No.4, 2012, pp. 476–478.

[49] G. Swain, S. Sultana, J. Moma, K. Parida, Fabrication of Hierarchical Two-Dimensional MoS_2 Nanoflowers Decorated upon Cubic $CaIn_2S_4$ Microflowers: Facile Approach to Construct Novel Metal-Free p–n Heterojunction Semiconductors with Superior Charge Separation Efficiency, *Inorganic Chemistry*, Vol.57, No.16, 2018, pp. 10059–10071.

[50] C. Zhou, S. Wang, Z. Zhao, Z. Shi, S. Yan, Z. Zou, A Facet-Dependent Schottky-Junction Electron Shuttle in a $BiVO_4${010}–Au–Cu_2O Z-Scheme Photocatalyst for Efficient Charge Separation, *Advanced Functional Materials*, Vol.28, No.31, 2018, 1801214.

[51] M.S. Gui, W.D. Zhang, Y.Q. Chang, Y.X. Yu, One-step Hydrothermal Preparation Strategy for Nanostructured WO_3/Bi_2WO_6 Heterojunction with High Visible Light Photocatalytic Activity,

Chemical Engineering Science, Vol.197, 2012, pp. 283–288.

[52] J. Sun, L. Sun, N. Han, J. Pan, W. Liu, S. Bai, Y. Feng, R. Luo, D. Li, A. Chen, Ordered Mesoporous WO3/ZnO Nanocomposites with Isotype Heterojunctions for Sensitive Detection of NO2, *Sensors and Actuators B: Chemical*, Vol.285, 2019, pp. 68–75.

[53] J.H. Pan, W.I. Lee, Preparation of Highly Ordered Cubic Mesoporous WO3/TiO2 Films and Their Photocatalytic Properties, *Chemistry of Materials*, Vol.18, No.3, 2006, pp. 847–853.

[54] A.S. Rajpurohit, N.S. Punde, C.R. Rawool, A.K. Srivastava, Fabrication of High Energy Density Symmetric Supercapacitor Based on Cobalt-Nickel Bimetallic Tungstate Nanoparticles Decorated Phosphorus-Sulphur Co-Doped Graphene Nanosheets, *Chemical Engineering Science*, Vol.371, 2019, pp. 679–692.

[55] C. Zhang, H. Zhang, K. Zhang, X. Li, Q. Leng, C. Hu, Photocatalytic Activity of ZnWO4: Band Structure, Morphology and Surface Modification, *ACS Applied Materials & Interfaces*, Vol.6, No.16, 2014, pp. 14423–14432.

[56] J. Li, C. Guo, L. Li, Y. Gu, K.B. Hee, J. Huang, In Situ Fabrication of 1D WO3 Nanorod/2D ZnWO4 Nanosheet Heterojunction for Enhanced Photoelectrochemical Performance, *Catalysis Letters*, Vol.152, No.1-3, 2022, pp. 1611–1620.

[57] A. Hsini, M. Benafqir, Y. Naciri, M. Laabd, A. Bouziani, M. Ez-zahery, R. Lakhmiri, N. El Alem, A. Albourine, Synthesis of an Arginine-Functionalized Polyaniline@FeOOH Composite with High Removal Performance of Hexavalent Chromium Ions from Water: Adsorption Behavior, Regeneration and Process Capability Studies, *Colloids and Surfaces A: Physicochemical and Engineering Aspects*, Vol.617, 2021, 126274.

[58] P.P. Liu, X. Liu, X.H. Huo, Y. Tang, J. Xu, H. Ju, TiO2–BiVO4 Heterostructure to Enhance Photoelectrochemical Efficiency for Sensitive Aptasensing, *ACS Applied Materials & Interfaces*, Vol.9, No.32, 2017, pp. 27185-27192.

[59] L. Ge, C. Han, J. Liu, In Situ Synthesis and Enhanced Visible Light Photocatalytic Activities of Novel PANI–g-C3N4 Composite Photocatalysts, *Journal of Materials Chemistry*, Vol.22, 2012, pp. 11843-11850.

[60] F. Wang, X: Liu, X., S. Hou, Z. Yang, K. Zhao, M. Zhang, Characterization and Performance Study of GR/ZnWO4 and MoS2/ZnWO4 Nanocomposite Photocatalysts, *Journal of Materials Science: Materials in Electronics*, Vol.34, 2023, Article Number 291.

[61] B. Barik, M. Mishra, P. Dash, Ionic Liquid-assisted Synthesis of a Novel PANI/ZnWO4/WO3 Ternary Nanocomposite: A Facile Double Electron Transfer Photocatalyst for Efficient Degradation of an Herbicide, *Environmental Science: Nano*, Vol.8, No.9, 2021, pp. 2676-2692.

[62] G. Ciri´c-Marjanovi´c, Recent Advances in Polyaniline Research: Polymerization Mechanisms, Structural Aspects, Properties and Applications, *Synthetic Metals*, Vol.177, 2013, pp. 1–47.

[63] S. Tan, J. Zhai, B. Xue, M. Wan, Q Meng, Y. Li, L. Jiang, D. Zhu, Property Influence of Polyanilines on Photovoltaic Behaviors of Dye-Sensitized Solar Cells, *Langmuir*, Vol.20, 2004, 2934–2937.

[64] N. Kumari Jangid, S. Jadoun, N. Kaur, A Review on High-throughput Synthesis, Deposition of Thin Films and Properties of Polyaniline, *European Polymer Journal*, Vol.125, 2020, 109485.

[65] B. Lange, *LUMISmini, Operating Manual*, Düsseldorf, Germany: Dr Bruno LANGE, 1994.

[66] B. Lange, *Vibrio fischeri -Microtox LCK 491 Kit*, Germany: Dr LANGE, 2010.

[67] W.C. Lipps, E.B. Braun-Howland, T.E. Baxter, *Standard Methods for the Examination of Water and Wastewater*, (24th. Edition). W.C. Lipps, E.B., Braun-Howland, T.E. Baxter, (editors), American Public Health Association (APHA), American Water Works Association (AWWA), Water Environment Federation (WEF), Elevate Your Standards. American Public Health Association 800 I Street, NW Washington DC: 20001-3770, United States, December 1, 2022; ISBN:9780875532998.

[68] B. Lange, *LUMIXmini Type Luminometer*, Dusseldorf: Dr LANGE Company, 1996.

[69] F. Siddique, S. Gonzalez-Cortes, A. Mirzaei, T. Xiao, M.A. Rafiq, X. Zhang, Solution Combustion Synthesis: The Relevant Metrics for Producing Advanced and Nanostructured Photocatalysts, *Nanoscale,* Vol.14, No.33, 2022, pp. 11806-11868.

Contribution of Individual Authors to the Creation of a Scientific Article (Ghostwriting Policy)

Sources of Funding for Research Presented in a Scientific Article or Scientific Article Itself

Conflict of Interest

The authors have no conflicts of interest to declare that are relevant to the content of this article.

Creative Commons Attribution License 4.0 (Attribution 4.0 International, CC BY 4.0)

Rukiye Öztekin, Delia Teresa Sponza

APPENDIX

Table 1. The initial experimental conditions for this study.

PANI/ZnWO$_4$/WO$_3$ NCs Concentrations (mg/l)	PANI/ZnWO$_4$/WO$_3$ Mass Ratios	GLP Concentrations (mg/l)	Photodegradation Time (min)	Solar Light Powers (W/m^2)
0.1	1:1:3	1	2	20
0.4	1:2:3	2	10	40
0.6	3:1:1	3	15	60
1.0	3:2:1	4	20	80
1.5				100
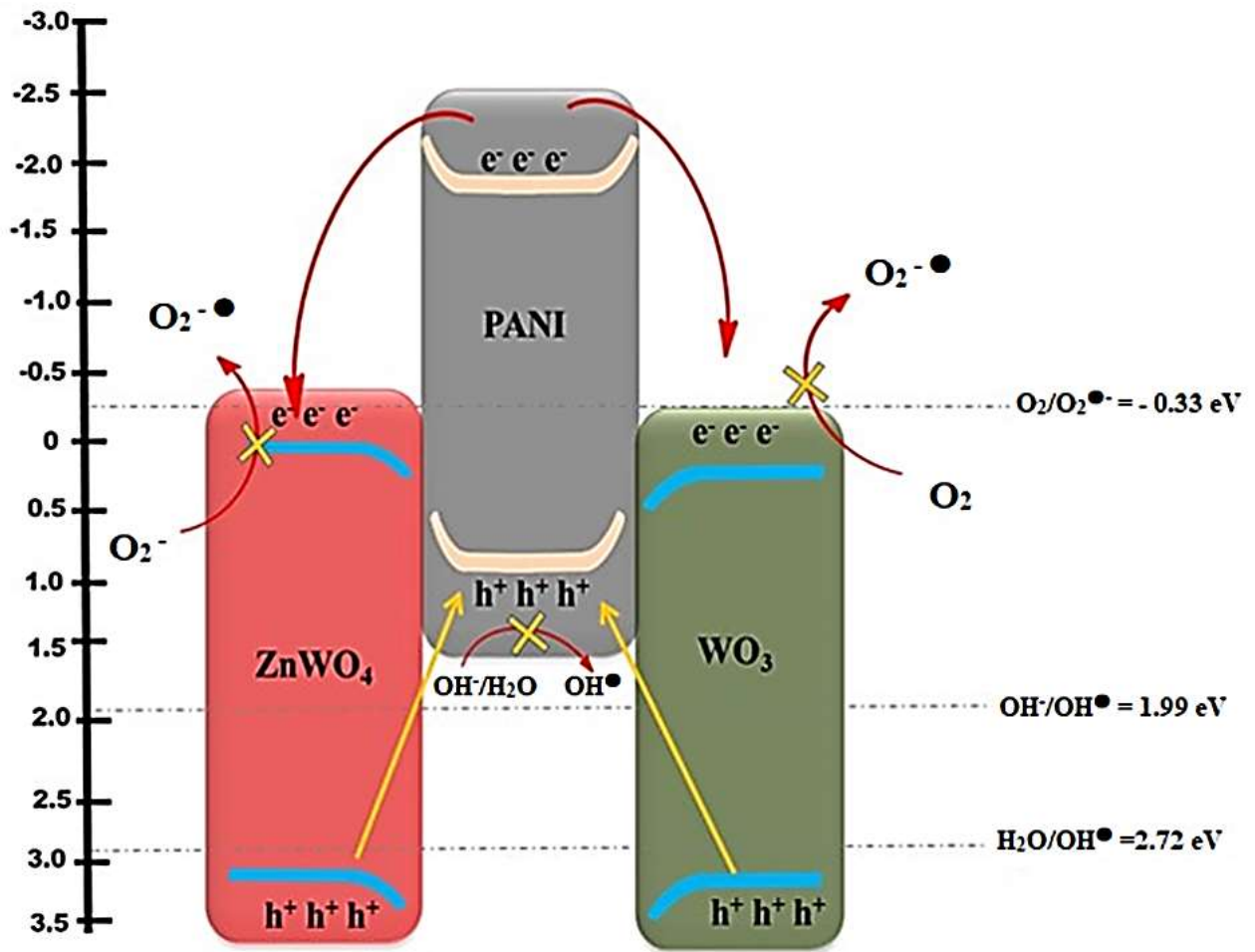
Fig. 1. Photodegradation Mechanism of PANI/ZnWO$_4$/WO$_3$ NCs
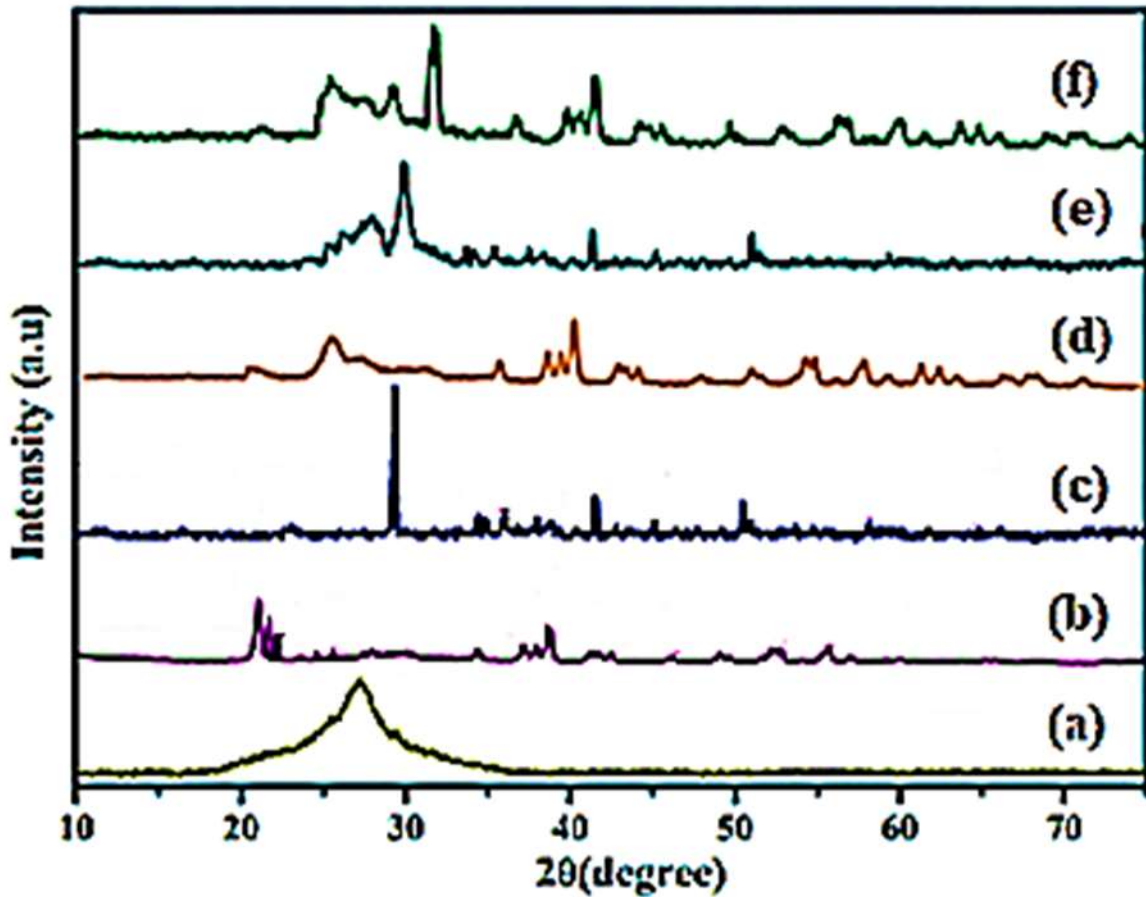
Fig. 2. The XRD patterns of **(a)** PANI, **(b)** WO_3 NPs, **(c)** $ZnWO_4$ NPs, **(d)** PANI-WO_3 NCs, **(e)** PANI-$ZnWO_4$ NCs and **(f)** PANI/$ZnWO_4$/WO_3 NCs, respectively, in surface water after photocatalytic degradation process for GLP removal.
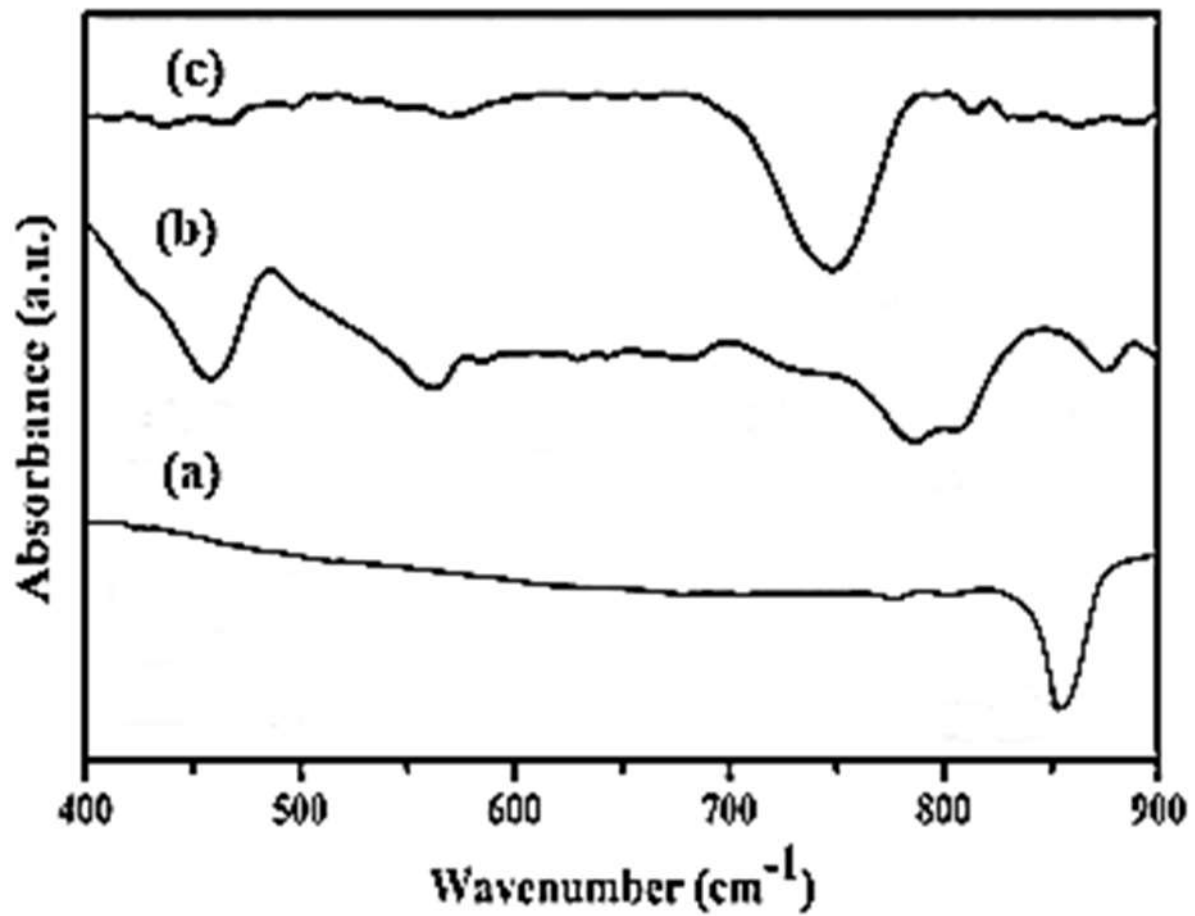
Fig. 3. FTIR spectrum of **(a)** PANI, **(b)** $ZnWO_4$ NPs and **(c)** WO_3 NPs, respectively, in surface water after photocatalytic degradation process for GLP removal.
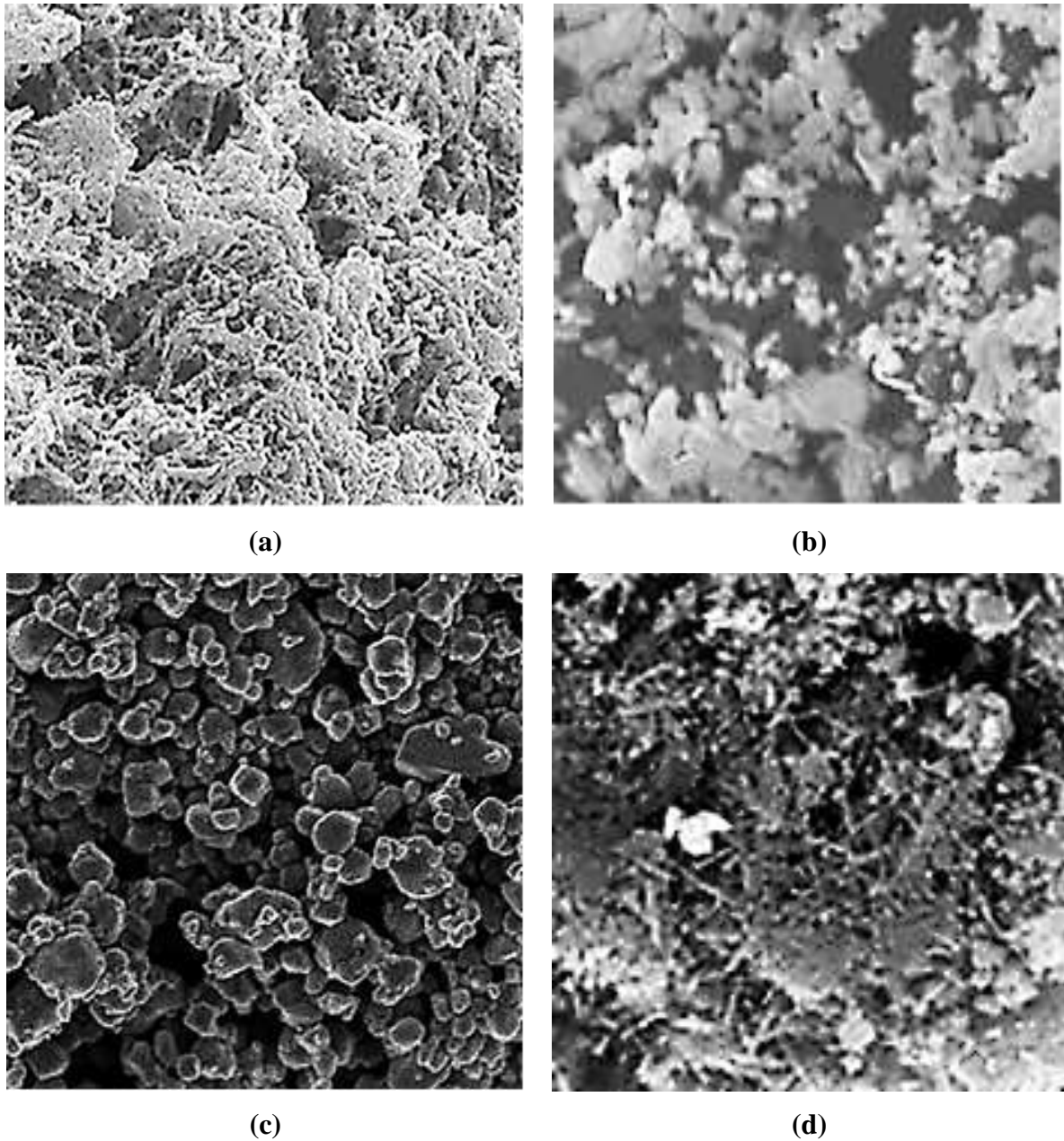
Fig. 4. FESEM images of **(a)** PANI, **(b)** $ZnWO_4$ NPs, **(c)** WO_3 NPs and **(d)** PANI//$ZnWO_4$/WO_3 NCs, respectively, in surface water after photocatalytic degradation process for GLP removal (FESEM images scale: 200 nm).
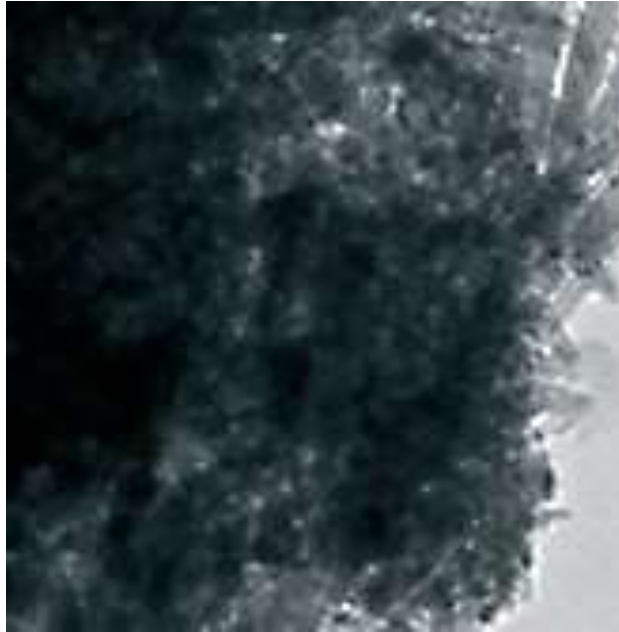
Rukiye Öztekin, Delia Teresa Sponza

Fig. 5. HRTEM images of PANI/ZnWO$_4$/WO$_3$ NCs in micromorphological structure level in surface water after photocatalytic degradation process for GLP removal (HRTEM image scale: 200 nm).
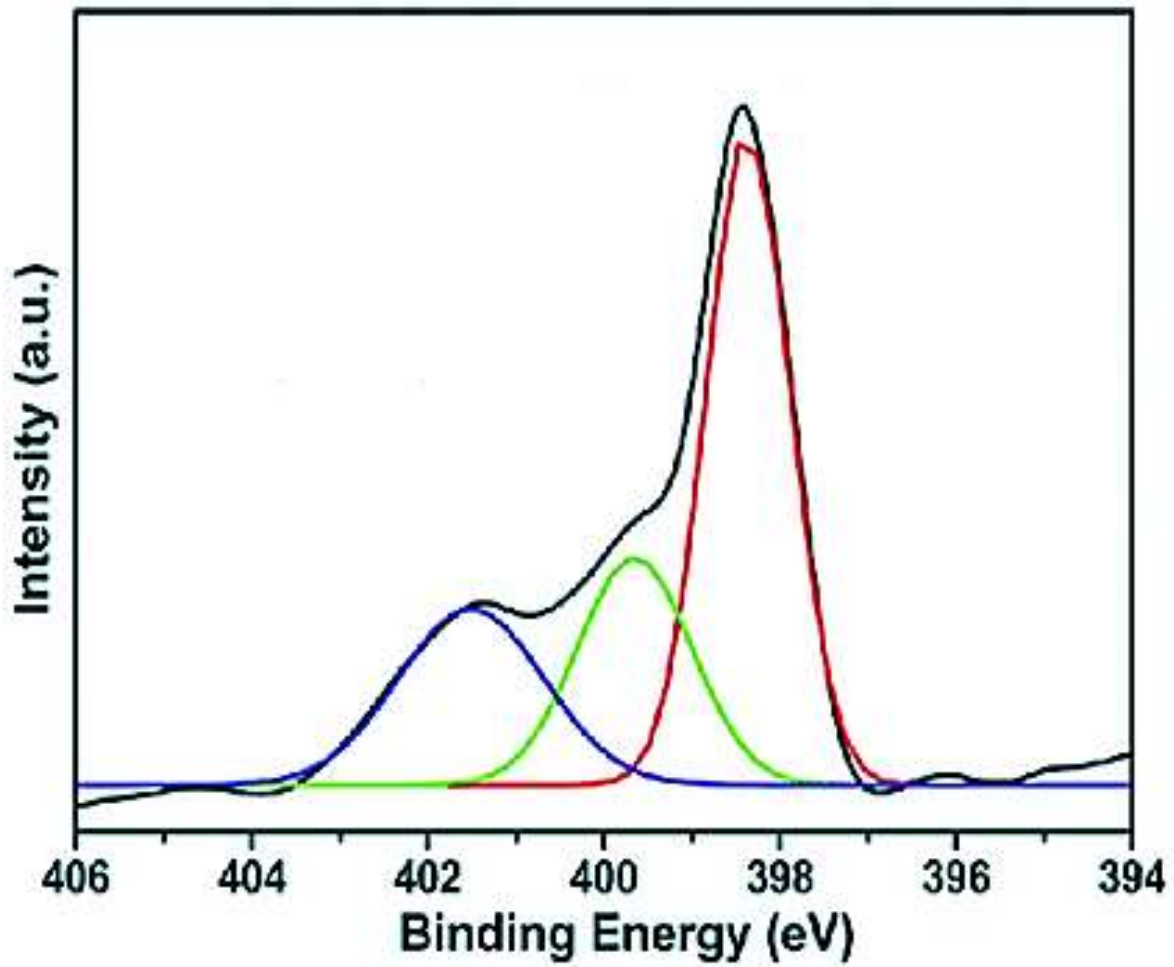
Fig. 6. The XPS spectra of **(a)** PANI (red) **(b)** ZnWO$_4$ NPs (green), **(c)** WO$_3$ (blue) and **(d)** PANI/ZnWO$_4$/WO$_3$ NCs (black), respectively, in surface water after photocatalytic degradation process for GLP removal.
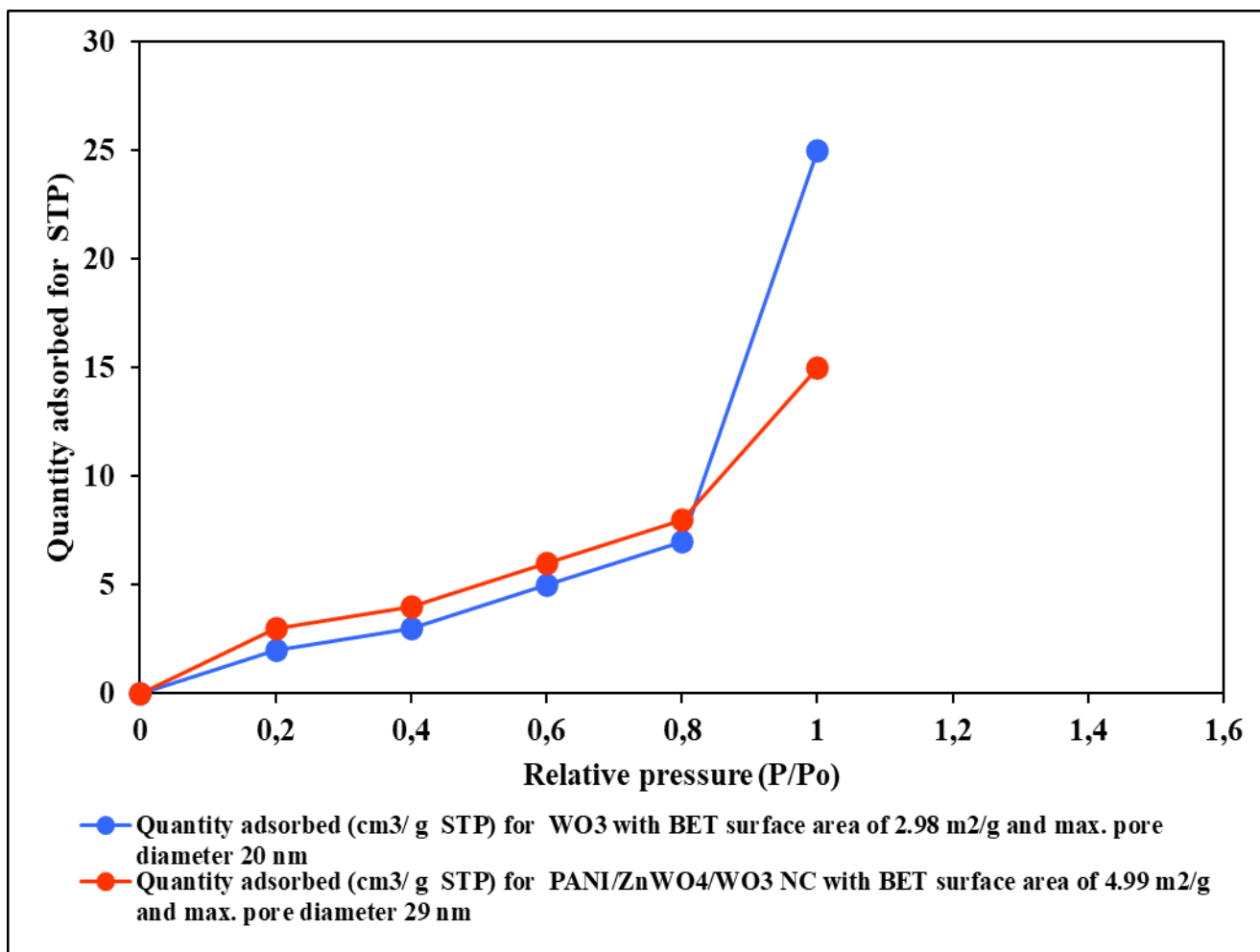
Rukiye Öztekin, Delia Teresa Sponza

Fig 7. N_2 adsorption desorption isoterm of PANI, $ZnWO_4$, WO_3 and PANI/$ZnWO_4$/WO_3 NCs

Rukiye Öztekin, Delia Teresa Sponza
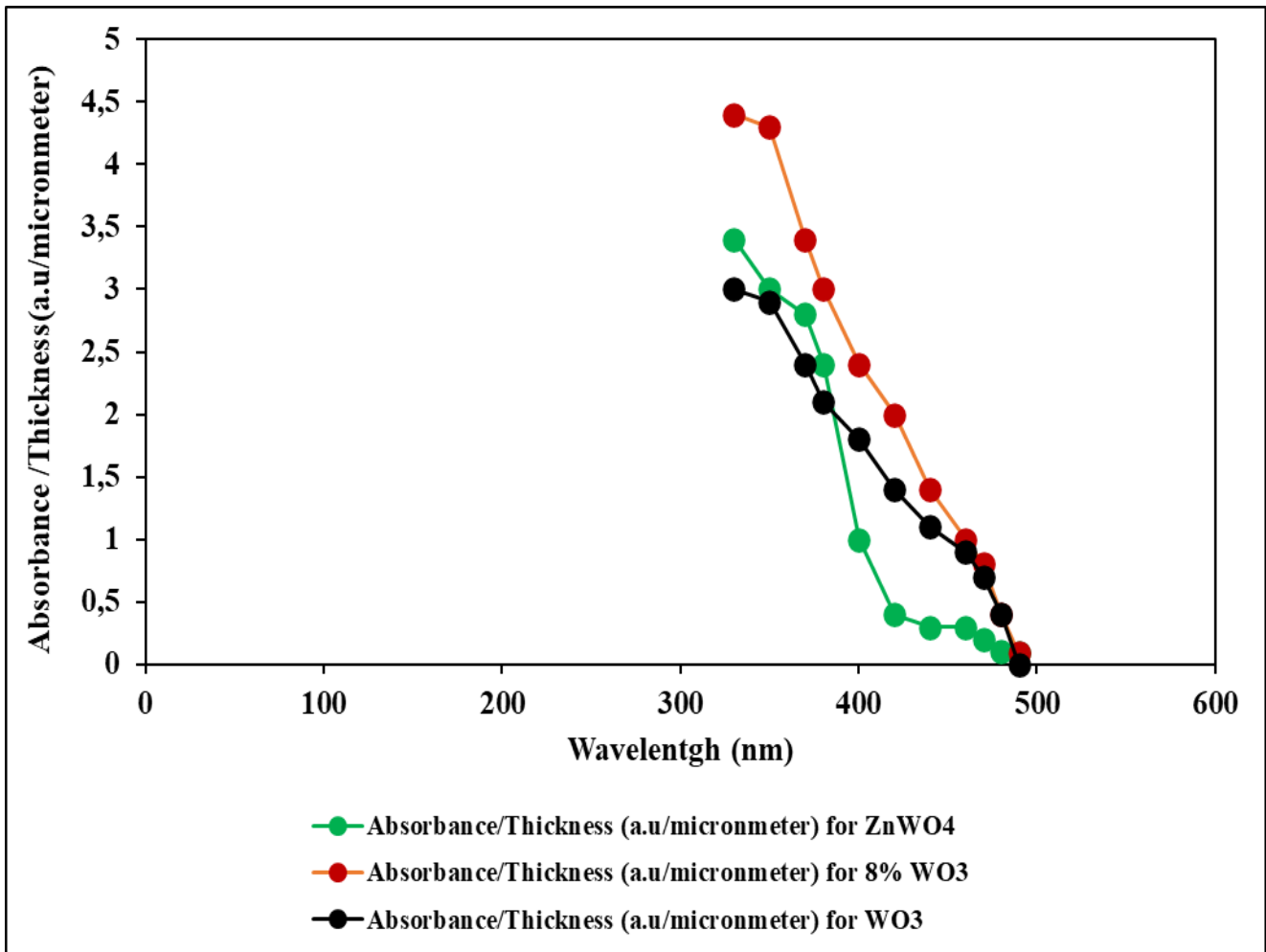
Fig 8a. UV−vis absorbance for WO_3, 8% Zn/WO_3, and $ZnWO_4$
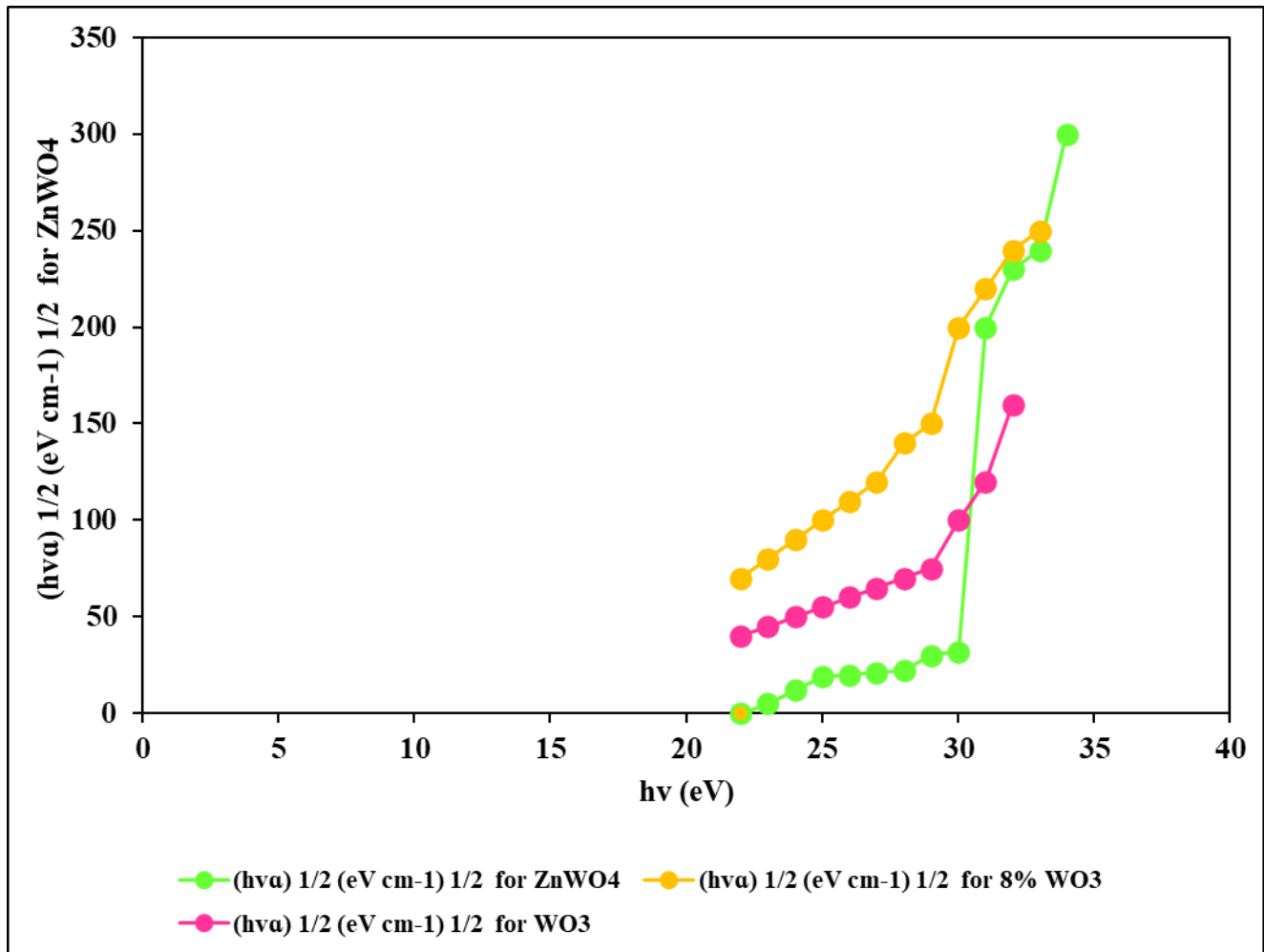
Fig 8b. Tauc plots for WO$_3$, ZnWO$_4$ and 8% WO$_3$
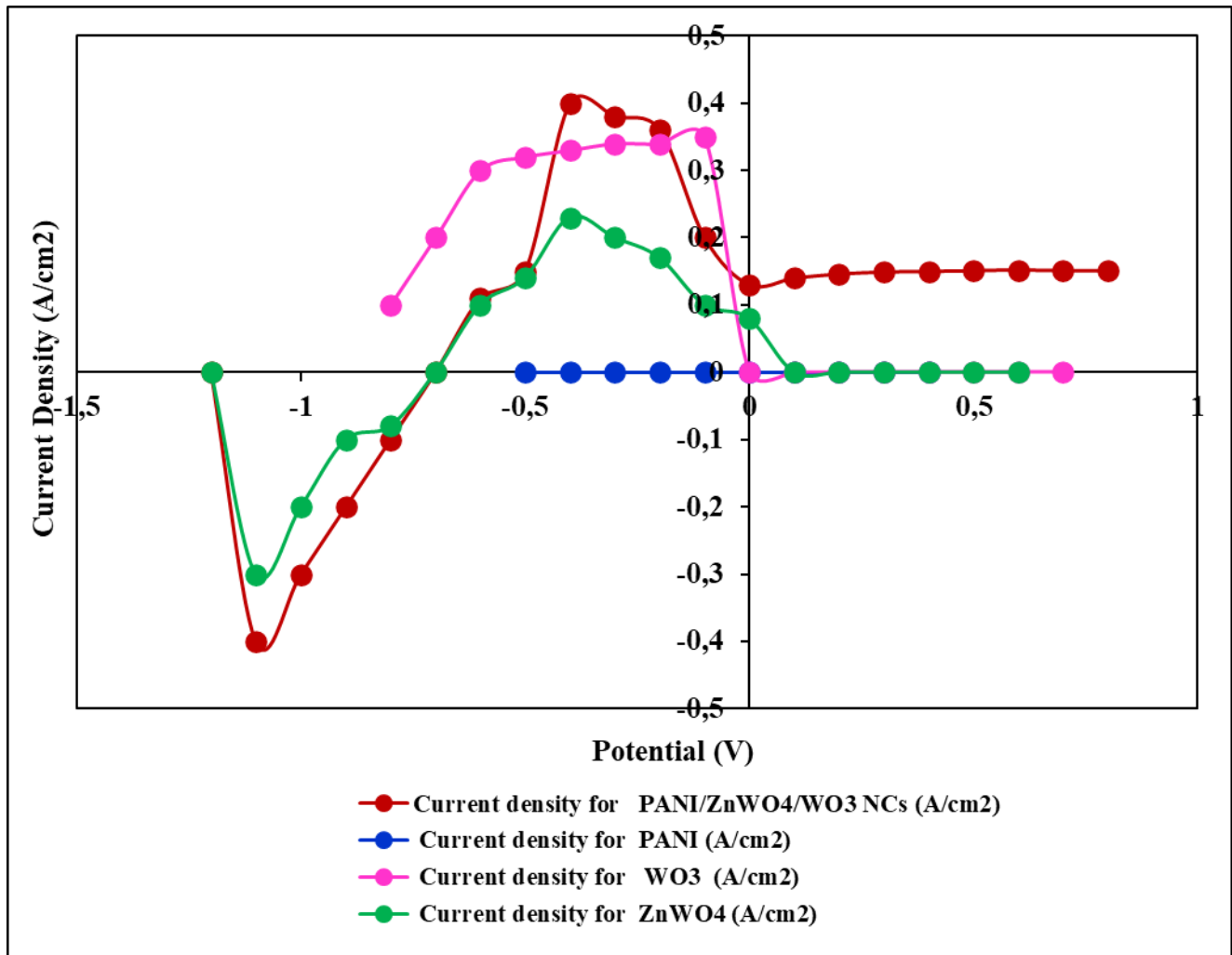
Fig 9. Cyclic voltammogram data of WO_3, PANI, $ZnWO_4$ and PANI/$ZnWO_4$/WO_3 NCs in 0.7 M $LiClO_4$-PC electrolyte.
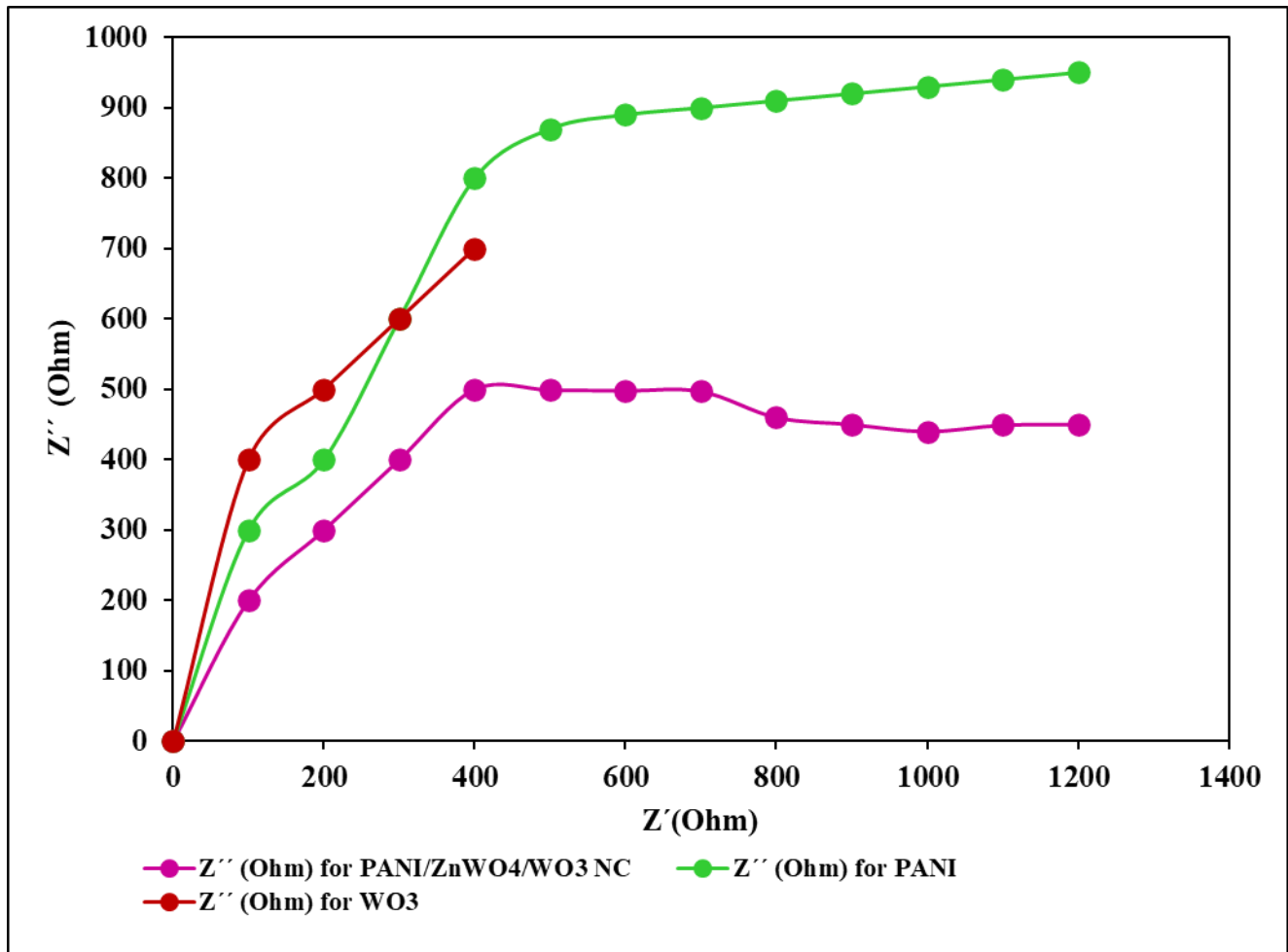
Fig. 10. Nyquist plots of WO$_3$, PANI, and PANI/ZnWO$_4$/ WO$_3$ NCs in 0.7 M LiClO$_4$-PC electrolyte
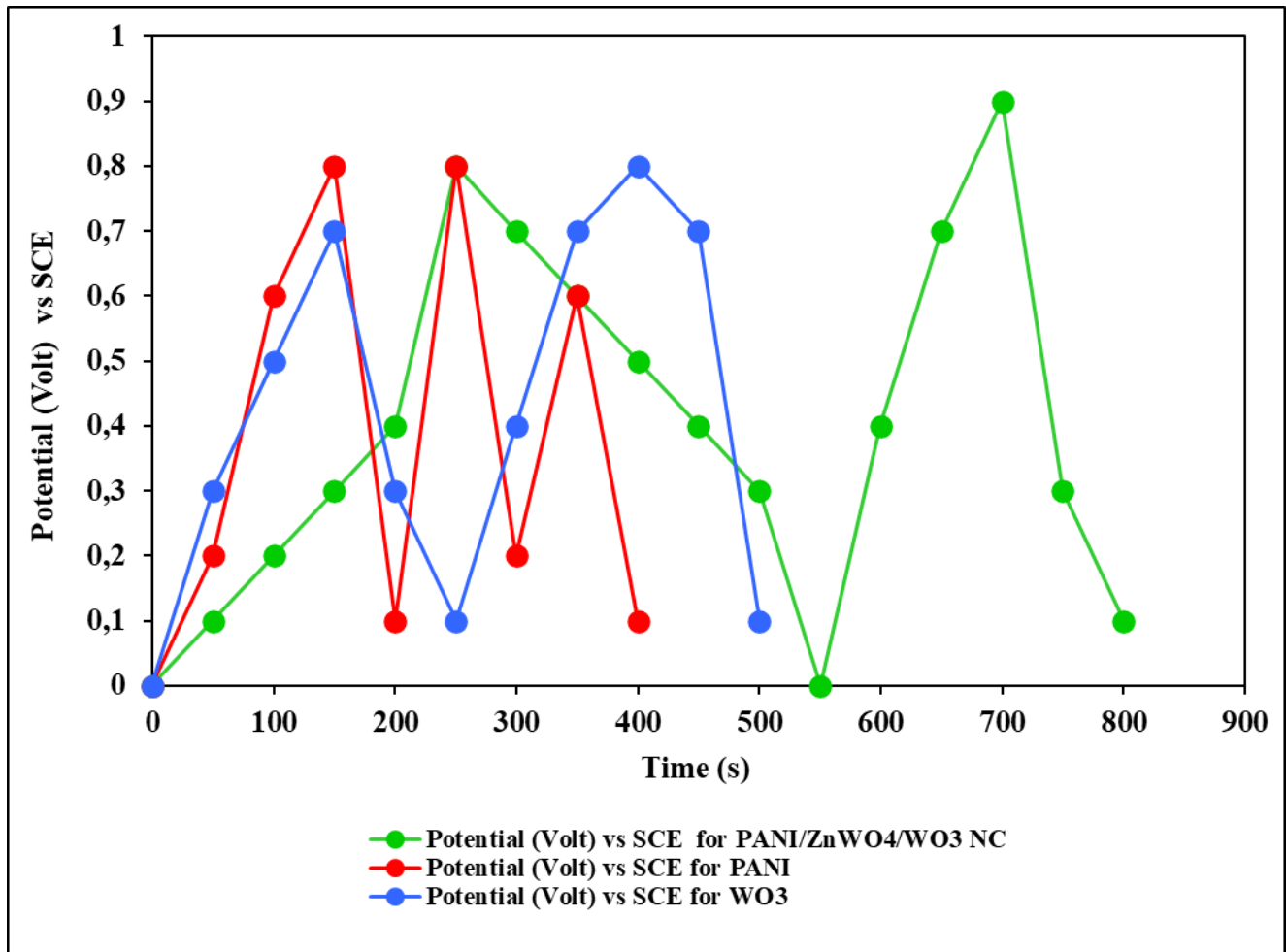
Rukiye Öztekin, Delia Teresa Sponza

Fig. 11a. Galvanostatic charge/discharge curve of PANI/WO$_3$ and PANI/ZnWO$_4$/WO$_3$ NCs
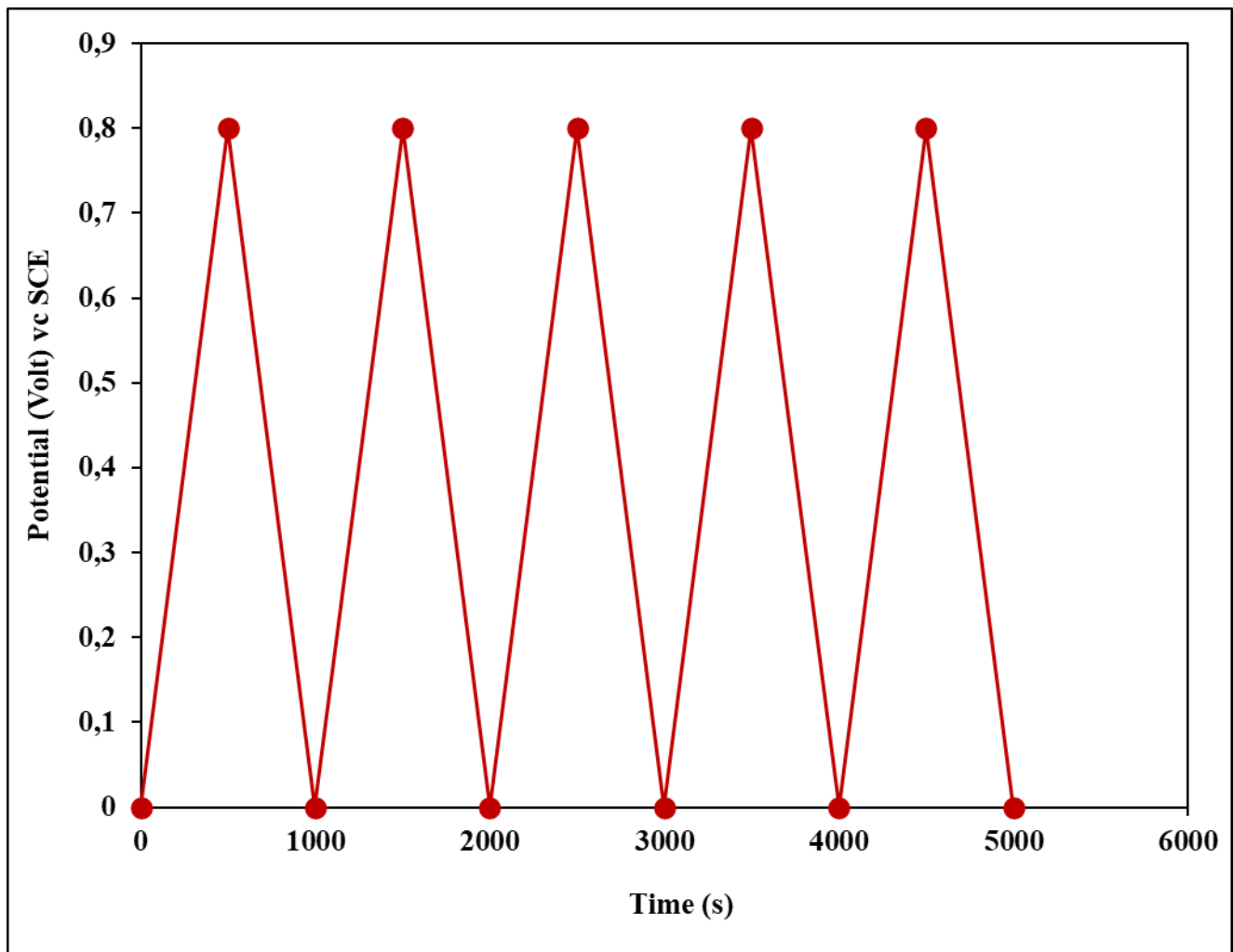
Fig. 11b. Galvanostatic charge/discharge curve of PANI/WO$_3$ NCs

Table 2. The effect of increasing PANI/ZnWO$_4$/WO$_3$ NCs concentrations for GLP removal

PANI/ZnWO$_4$/WO$_3$ NCs Concentrations (mg/l)	GLP Removal Efficiency (%)
0.1	68
0.4	74
0.6	80
1.0	99
1.5	91

Table 3. The effect of different PANI/ZnWO$_4$/WO$_3$ mass ratios for GLP removal

PANI/ZnWO$_4$/WO$_3$ Mass Ratios	GLP Removal Efficiency (%)
1:1:3	67
1:2:3	99
3:1:1	86
3:2:1	79

Table 4. The effect of different GLP concentrations for GLP removal

GLP Concentrations (mg/l)	GLP Removal Efficiency (%)
1	65
2	82
3	99
4	84

Table 5. The effect of increasing photodegradation time for GLP removal

Photodegradation Time (min)	GLP Removal Efficiency (%)
2	68
10	81
15	99
20	73

Table 6. The effect of increasing solar light power for GLP removal

Solar Light Power (W/m^2)	GLP Removal Efficiency (%)
20	58
40	71
60	86
80	99
100	92

Table 7. Effect of increasing GLP concentrations on Microtox acute toxicity in surface water after photocatalytic degradation process, at 30ºC and at 60ºC.

No	Parameters	Microtox Acute Toxicity Values, * EC (mg/l)							
		25ºC							
		0. min		60. min		120. min		180. min	
		*EC$_{90}$		*EC		*EC		*EC	
1	Control	825		EC$_{70}$=510		EC$_{60}$=650		EC$_{49}$=638	
		30ºC				60ºC			
		0. min	60. min	120. min	180. min	0. min	60. min	120. min	180. min
		*EC$_{90}$	*EC	*EC	*EC	*EC$_{90}$	*EC	*EC	*EC
2	Control	825	EC$_{70}$=580	EC$_{50}$=580	EC$_{39}$=548	825	EC$_{55}$=550	EC$_{40}$=590	EC$_{29}$=688
3	GLP=1 mg/l	825	EC$_{62}$=422	EC$_{27}$=242	EC$_{17}$=168	825	EC$_{57}$=419	EC$_{22}$=266	EC$_{12}$=150
	GLP=2 mg/l	825	EC$_{62}$=421	EC$_{27}$=239	EC$_{17}$=167	825	EC$_{57}$=414	EC$_{22}$=232	EC$_{12}$=161
	GLP=3 mg/l	825	EC$_{57}$=414	EC$_{22}$=236	EC$_{12}$=16.5	825	EC$_{52}$=550	EC$_{17}$=214	EC$_{7}$=5
	GLP=4 mg/l	825	EC$_{67}$=408	EC$_{32}$=230	EC$_{22}$=162	825	EC$_{62}$=403	EC$_{27}$=218	EC$_{17}$=148
* EC values were calculated based on COD$_{dis}$ (mg/l). Control: raw ww.									

Table 8. Effect of increasing GLP concentrations on *Daphnia magna* acute toxicity in surface water after photocatalytic degradation process, at 30ºC and at 60ºC.

No	Parameters	*Daphnia magna* Acute Toxicity Values, * EC (mg/l)							
		25ºC							
		0. min		60. min		120. min		180. min	
		*EC$_{50}$		*EC		*EC		*EC	
1	Control	850		EC$_{45}$=625		EC$_{40}$=370		EC$_{29}$=153	
		30ºC				60ºC			
		0. min	60. min	120. min	180. min	0. min	60. min	120. min	180. min
		*EC$_{50}$	*EC	*EC	*EC	*EC$_{50}$	*EC	*EC	*EC
2	Control	850	EC$_{39}$=468	EC$_{34}$=228	EC$_{23}$=111	850	EC$_{34}$=373	EC$_{29}$=210	EC$_{18}$=71
3	GLP=1 mg/l	850	EC$_{32}$=450	EC$_{22}$=145	EC$_{17}$=260	850	EC$_{32}$=130	EC$_{17}$=425	EC$_{12}$=340
	GLP=2 mg/l	850	EC$_{37}$=450	EC$_{22}$=175	EC$_{17}$=100	850	EC$_{32}$=425	EC$_{17}$=140	EC$_{7}$=90
	GLP=3 mg/l	850	EC$_{32}$=350	EC$_{17}$=240	EC$_{12}$=90	850	EC$_{27}$=150	EC$_{12}$=60	EC$_{7}$=6
	GLP=4 mg/l	850	EC$_{42}$=300	EC$_{27}$=170	EC$_{22}$=52	850	EC$_{37}$=250	EC$_{22}$=110	EC$_{17}$=11
* EC values were calculated based on COD$_{dis}$ (mg/l). Control: Raw ww									